THE ASTROPHYSICAL JOURNAL, 388:467–488, 1992 April 1

SYNTHESIS IMAGING OF THE DR 21 (OH) CLUSTER. II. THERMAL AMMONIA AND WATER MASER EMISSION

JEFFREY G. MANGUM
Department of Astronomy, The University of Texas, Austin, TX 78712; and National Radio Astronomy Observatory[1]
ALWYN WOOTTEN
National Radio Astronomy Observatory,[1] Edgemont Road, Charlottesville, VA 22903
AND
LEE G. MUNDY
Astronomy Program, University of Maryland, College Park, MD 20742
Received 1991 August 5; accepted 1991 October 1

ABSTRACT

High-sensitivity, 4″ resolution images of the thermal ammonia and water maser emission have been made of the DR 21 (OH) molecular cloud. Images of the NH_3(1, 1) and (2, 2) transitions show four primary emission regions embedded in a generally clumpy emission distribution. A total of 18 ammonia cores are identified in these images. An analysis of the physical properties of these cores has shown that they are massive ($M_G \simeq$ 15–1000 $M_\odot$) and warm ($T_K \simeq 20$ to greater than 80 K) with a range of sizes ($\theta_S \simeq 0.06$–0.28 pc). One of these cores is a hot ($T_K > 80$ K), compact ($\theta_S \simeq 0.07$ pc) region associated with shell-type H_2O maser emission. The three-dimensional distribution of these cores suggests a strong interaction between young massive stars and their maternal environs. Two source concepts are formulated to explain this distribution.

Analysis of the observed distribution of NH_3 core mass shows that the mass spectrum follows a power law, $dN/dM \propto M^{-\alpha}$, with $\alpha \gtrsim 0.7$, consistent with previous determinations. A comparison between the virial masses in Taurus, OMC 1/OMC 2, and DR 21 (OH) has been made. OMC 1/OMC 2 and DR 21 (OH) have similar star-forming core properties, which are very different from those found in Taurus. Core virial mass seems to represent a fundamental distinction between low- and high-mass star formation.

Subject headings: ISM: individual [DR 21 (OH)] — ISM: molecules — ISM: structure

1. INTRODUCTION

The DR 21 H II region, the most intense 5 GHz continuum source in the Cygnus X complex (Downes & Rinehart 1966; Harris 1973), is one of the best-studied star forming regions in the galaxy. DR 21 contains a cluster of late-type O stars (Roelfsema, Goss, & Geballe 1989) and one of the most intense stellar outflows known (Lane et al. 1990; Garden et al. 1986; Fischer et al. 1985). Coupled with its relative proximity (3 kpc; Campbell et al. 1982), the DR 21 region presents the astrophysicist with a perfect location in which to study the violent interaction between young stars and their maternal environment.

Approximately 2.6 pc ($\sim 3'$) to the north of DR 21 is a dense molecular region which harbors what appears to be a cluster of young forming stars (Woody et al. 1989; Mangum, Wootten, & Mundy 1991, hereafter Paper I). In Paper I, we presented 7″ resolution observations of the 2.7 mm continuum and $J = 1 \rightarrow 0$ $C^{18}O$ emission toward DR 21 (OH) which showed that the molecular cloud core is composed of three compact emission regions, all of which appear to be actively forming stars. DR 21 (OH), like DR 21, appears to be a massive star-forming region, but unlike DR 21, the forming stars in DR 21 (OH) have not disrupted their parent cloud, and offer a glimpse of an earlier state in the evolution of a star-forming region.

In order to further characterize the density, temperature, and dynamical structure on scales of less than 0.1 pc, we have made high-resolution high-sensitivity measurements of the thermal NH_3(1, 1) and (2, 2) and the H_2O maser emission toward DR 21 (OH).

2. OBSERVATIONS

2.1. NH_3 (1, 1) *and* (2, 2) *Emission*

Observations of the (1, 1) and (2, 2) rotation-inversion transitions of NH_3 were made on 1988 September 9–10 using the NRAO Very Large Array. The 27 antennas were in the D-configuration during these observations. Sixty-four spectral channels were used to sample the 3.125 MHz IF bandwidth which, after on-line Hanning smoothing, resulted in a frequency resolution and channel spacing of 48.828 kHz. This observing setup allowed us to measure both transitions simultaneously by using two IFs. In order to sample the emission from the main, inner satellite, and outer satellite hyperfine components of the (1, 1) transition, the first IF was tuned to a frequency of 23.6952733 GHz. The second IF was set at a rest frequency of 23.7232813 GHz to sample the emission from the main and inner satellite hyperfine components of the (2, 2) transition. The center channel LSR velocity was set at -3.0 km s^{-1} which, given the velocity resolution of 0.62 km s^{-1}, yielded a total velocity coverge of $-32.3 \leq V_{LSR} \leq 6.6$ km s^{-1} for the (1, 1) transition and $-30.6 \leq V_{LSR} \leq 8.2$ km s^{-1} for the (2, 2) transition. DR 21 (OH) was observed with an antenna pointing position of $\alpha(1950) = 20^h37^m14^s.0$, $\delta(1950) = 42°12'00''$. The phase calibration source was 2005+403 (measured flux density 3.7 Jy). To establish the flux density

[1] The National Radio Astronomy Observatory is operated by Associated Universities, Inc., under cooperative agreement with the National Science Foundation.

scale, an observation of 3C 286 (assumed flux density 2.42 Jy) was made. The accuracy of the flux density calibration is ~5%. An observation of 3C 273 (measured flux density 32.8 Jy) was used to calibrate the bandpass. The antenna amplitudes and phases were calibrated within AIPS.

Since the strong continuum source DR 21 is located 180″ south of our antenna pointing position, placing it just beyond the first null of the antenna primary beam (FWHM = 1.′9), we found it necessary to remove the map distortions due to this source. To effect this removal, we constructed a model of DR 21 using the CLEAN algorithm in AIPS. This CLEAN model was then subtracted from the entire *u-v* data set.

Maps of each spectral line channel were made with natural weighting and no tapering of the *u-v* data. The resulting synthesized beam size was 4.″0 × 3.″4, position angle −81°. Ten channels in the first IF [containing the (1, 1) transition] and 24 channels in the second IF [containing the (2, 2) transition] were found to be devoid of emission. These line-free channels were averaged in each IF to form line-free continuum maps which were subtracted from the line channel maps. Even though continuum emission at the 2 σ level may be present we estimate that there is no continuum emission in these averaged line-free continuum maps to a 3 σ limit of 15 mJy beam^{-1}. After this dirty map continuum subtraction, each spectral line channel was CLEANed in the usual manner. All maps were then corrected for the response of the primary beam. The rms noise in these CLEANed maps was 10 mJy beam^{-1}, which corresponds to a main-beam brightness temperature of 1.6 K (K/Jy = 163).

2.2. H_2O *Maser Emission*

Observations of the $6_{16} \rightarrow 5_{23}$ transition of H_2O (rest frequency 22.2351179 GHz) were made on 1988 December 19 using the NRAO Very Large Array in the A-configuration with 27 antennas. The total observing bandwidth of 3.125 MHz was divided into 128 spectral line channels with a frequency resolution and channel spacing of 24.4 kHz (0.33 km s^{-1} at the line rest frequency). The center channel LSR velocity was set at −3.0 km s^{-1}, which yielded a total velocity coverage of $-23.7 \leq V_{LSR} \leq 17.7$ km s^{-1}. The flux density scale was established by assuming a flux of 3.7 Jy for 2005+403. DR 21 (OH) was observed at an antenna pointing and phase center position of $\alpha(1950) = 20^h37^m14^s.0$, $\delta(1950) = 42°12'13''$. The phase calibration source was 2005+403. An observation of 3C 84 (measured flux 53.7 Jy) was used to calibrate the bandpass. The antenna amplitudes and phases were calibrated within AIPS.

To correct for the antenna-based amplitude and phase errors in this high signal-to-noise data set, one spectral line channel was mapped and CLEANed using the AIPS task MX and used as an input source model for self-calibration within the AIPS task CALIB. The self-calibrated spectral line channel produced by CALIB was then mapped and CLEANed with MX and used as a revised source model. This MX-CALIB cycle was repeated several times until a good fit to the raw *u-v* data was obtained. This self-calibration model was then applied to the entire spectral line *u-v* data set.

Maps of each spectral line channel were made using natural weighting and no tapering of the *u-v* data. The resulting synthesized beam size was 0.″079 × 0.″076, position angle −51°. Each spectral line channel was then CLEANed in the usual manner. The rms noise in the spectral channels devoid of maser emission was typically 10 mJy beam^{-1}.

3. RESULTS

3.1. NH_3 (1, 1) *and* (2, 2) *Emission*

Figures 1 and 2 show the individual channel maps from our NH_3 $\Delta F = 0$ (1, 1) and (2, 2) observations. In the (1, 1) transition we detected the $\Delta F = 0$ (main[2]), $F = 1 \rightarrow 2$, $F = 1 \rightarrow 0$, and part of the $F = 2 \rightarrow 1$ hyperfine components. We detected the $\Delta F = 0$ (main[2]) and, toward the peak position, also the $F = 2 \rightarrow 3$ hyperfine of the (2, 2) inversion transition. Integrated intensity images over each of the (1, 1) $\Delta F = 0$, $F = 1 \rightarrow 2$, $F = 1 \rightarrow 0$, and (2, 2) $\Delta F = 0$ hyperfine transitions are shown in Figure 3. In these images there are four "primary" emission sources embedded within an emsemble of "secondary" emission sources. These primary emission sources coincide both in position and LSR velocity with previously identified dust continuum and molecular spectral line sources (see §§ 4.2.1–4.2.4), while the secondary emission sources have no known counterparts. Following the nomenclature of Paper I, we shall refer to the primary sources as DR 21 (OH) N, DR 21 (OH) main (composed of MM 1 and MM 2), DR 21 (OH) W, and DR 21 (OH) S (see Fig. 3 for identifications). To show the spectral characteristics of each source, Figure 4 shows representative spectra taken through the peak NH_3(1, 1) $\Delta F = 0$ and (2, 2) $\Delta F = 0$ positions for each of these primary (and their main subcomponent) emission features. The selection criterion used to identify all of the NH_3 sources will be described in § 4.1.

To estimate the fraction of single antenna flux recovered by these observations, we compare our measurements with those of Mauersberger et al. (1985). In a 40″ beam Mauersberger et al. measure a peak main-beam brightness temperature of 5.7 and 4.0 K for the main (1, 1) $\Delta F = 0$ and (2, 2) $\Delta F = 0$ hyperfine transitions. These brightness temperatures correspond to fluxes of 4.2 and 3.0 Jy, respectively. By spatially integrating over a 40″ diameter region in the peak velocity channel of our (1, 1) $\Delta F = 0$ and (2, 2) $\Delta F = 0$ maps, we measure 4.4 and 2.9 Jy, indicating that we have recovered all of the single-antenna flux. In order to show the overall spectral characteristics of our observations, Figures 5 and 6 show (1, 1) and (2, 2) spectra made by spatially integrating over the primary beam (1.′9) in each spectral channel.

Since hyperfine intensity anomalies in the (1, 1) transition have been detected in several sources (Matsakis et al. 1977; Stutzki & Winnewisser 1985), we have searched for this effect in our data. Based on the model for this effect developed by Stutzki & Winnewisser (1985), the intensity of the $F = 0 \rightarrow 1$ hyperfine transition should appear much stronger than the $F = 1 \rightarrow 0$ hyperfine while the $F = 1 \rightarrow 2$ hyperfine component should appear to be only slightly stronger than the $F = 2 \rightarrow 1$ hyperfine component. One should also find that at $T_K > 30$ K the relative intensity of the $F = 1 \rightarrow 0$ hyperfine should drop below its LTE value of 0.22. Since the bandpass of our observations did not include the $F = 0 \rightarrow 1$ hyperfine transition, we can only look for anomalies in the $(F = 1 \rightarrow 2)/(F = 2 \rightarrow 1)$ ratio and the relative intensity of the $F = 1 \rightarrow 0$ hyperfine component. We find no evidence for anomalous hyperfine intensities in either of these comparisons. In the Stutzki & Winnewisser model, unresolved clumps of NH_3 with line widths of less than 0.3 km s^{-1} cause nonequal overlap between

[2] For observed line widths ≤90 kHz (≤1 km s^{-1}) the main hyperfine components of the (1, 1) and (2, 2) transitions separate into three $\Delta F = 0$ quadrupole hyperfine transitions (see Kukolich 1967; also our Figs. 5 and 6).

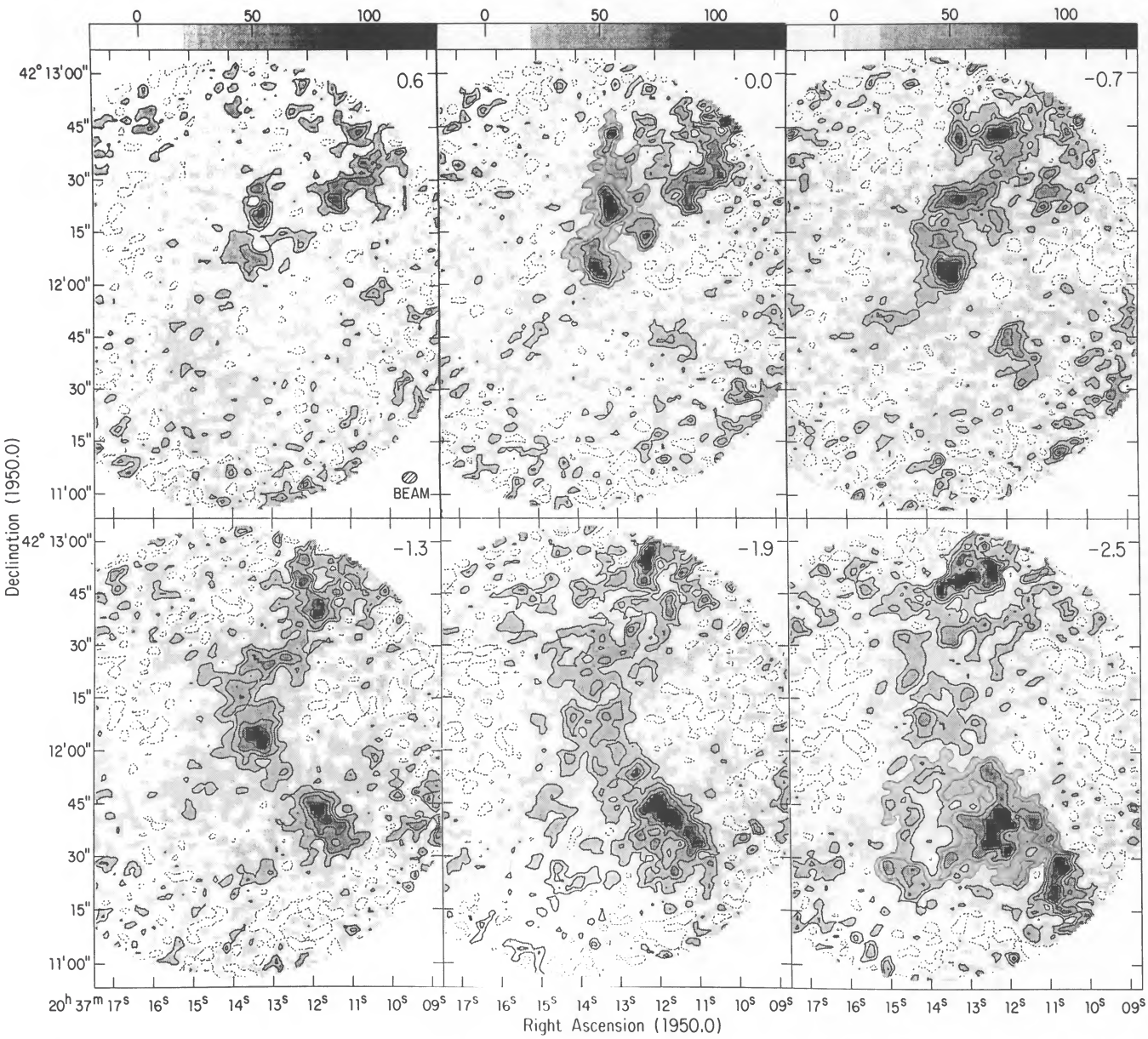

FIG. 1.—$NH_3(1, 1)$ $\Delta F = 0$ emission channel maps toward DR 21 (OH). The contours are -20, 20, 40, 60, 80, 100, and 120 mJy beam^{-1} (-3.2, 3.2, 6.4, 9.6, 12.8, 16.0, and 19.2 K), while the gray scale runs from -20 to 130 mJy beam^{-1} (-3.2 to 20.8 K). The LSR velocity with respect to the frequency of the (1, 1) $F = 2 \rightarrow 2$ quadrupole hyperfine transition for each channel and the synthesized beam are indicated.

the hyperfine transitions of the infrared (2, 1) $\rightarrow$ (1, 1) transition, which leads to a selective overpopulation in several of the hyperfine states of the (1, 1) transition. In the single-antenna observations of Mauersberger et al. (1985) the $NH_3(1, 1)$ hyperfine structure is not anomalous. Since the NH_3 clumps in our observations of DR 21 (OH) have line widths greater than ~ 1.2 km s^{-1} and, except for the warmest source (which also has the largest line width), have beam filling factors $\simeq 1$, it is not surprising that the $NH_3(1, 1)$ emission in DR 21 (OH) does not show anomalous hyperfine structure.

3.2. H_2O *Maser Emission*

A total of three H_2O maser emission groups were detected within the 1.9 primary beam of these observations. Figure 7 shows a comparison between a single-antenna H_2O maser spectrum of DR 21 (OH) obtained using the NRAO 43 m telescope and a spectrum produced from the interferometer observations. All of the features detected in the single antenna spectrum are evident in the interferometer observations. We also display in Figure 7 the contributions from each maser emission group to the total DR 21 (OH) water maser emission.

In order to determine the absolute positional accuracy of these interferometric H_2O maser measurements, we have analyzed four potential sources of positional uncertainty: the uncertainty in the position of the phase calibrator, uncertainties introduced by self-calibration, the positional stability of the data over the observing run, and the systematic uncertainty due to the difference between the source and phase calibrator positions. Of these four effects, the $\pm 0.''05$ uncertainty in the position of the phase calibrator (2005+403) is the largest,

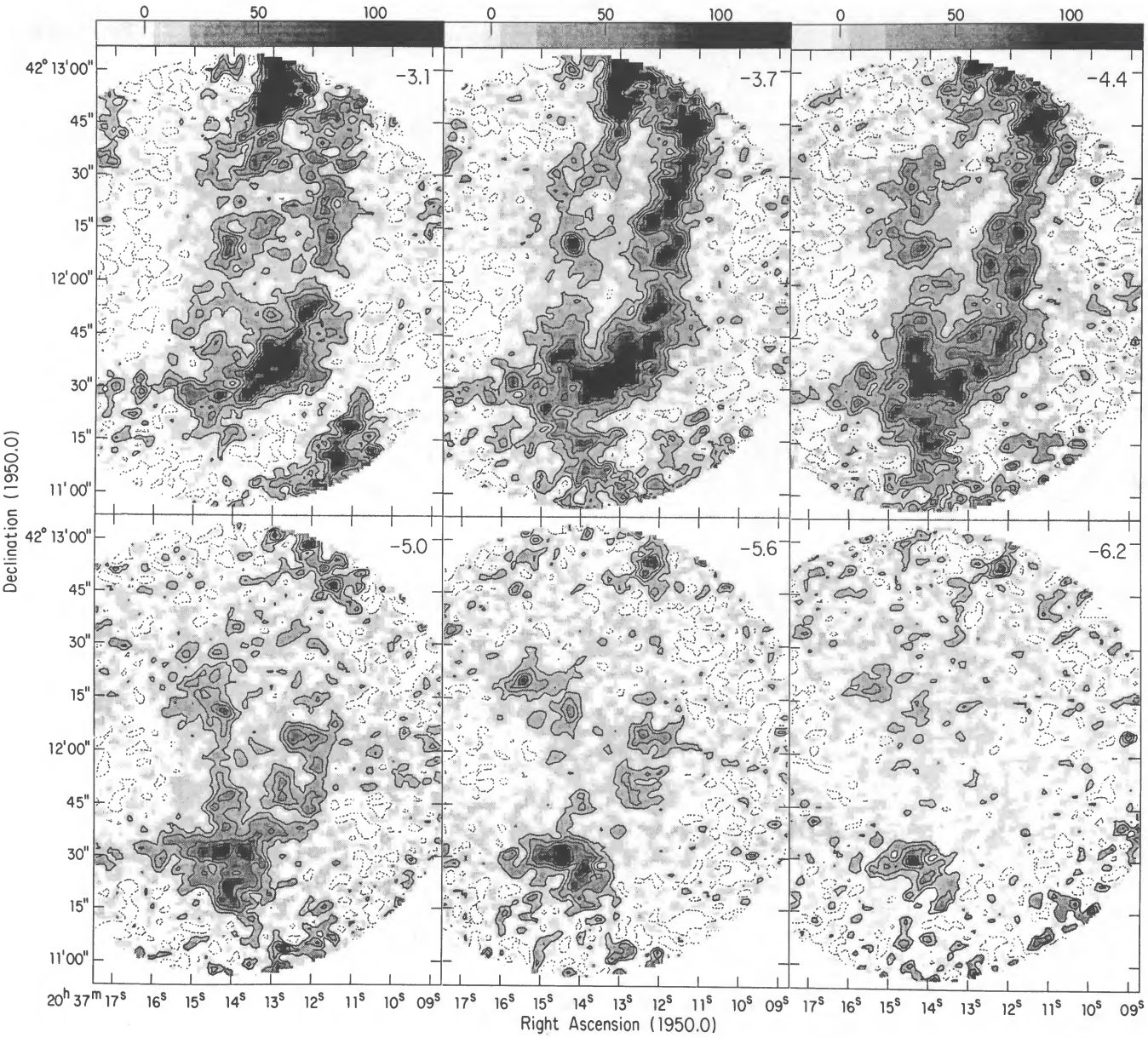

FIG. 1.—*Continued*

while the other three sources of uncertainty are $\lesssim 0''.02$. Therefore, we estimate that the absolute positions of the H_2O masers are accurate to $\pm 0''.05$.

By measuring the positional shifts of each maser emission center as a function of velocity, we find that each emission center is actually composed of several components. Table 1 lists the positions and properties of each emission center and their associated components. Note that even though our synthesized beam is $0''.077$, the high ($>100:1$) signal-to-noise ratio in these observations allows us to determine relative positions to a much higher accuracy. Assuming a Gaussian source, the 1 σ position uncertainty due to noise is $(0.45/\mathrm{SNR})\theta$ (Reid et al. 1988), where θ is the half-power width and SNR is the peak signal-to-noise ratio of the source. Since the observed maser components are unresolved, θ is just the synthesized beamwidth.

The velocity centroids for the emission groups listed in Table 1 are -3.77, 10.38, and -10.50 km s^{-1}. As can be seen from Figure 8, the maser group at -3.77 km s^{-1} is associated with the MM 1 NH_3 source, while the maser groups at 10.38 and -10.50 km s^{-1} are associated with MM 2. In the standard shell model for saturated masers (Reid et al. 1977; Genzel & Downes 1977), where H_2O maser emission arises in expanding shells around young massive stars, the velocity centroid for a maser emission group is the radial velocity of the central star. From our NH_3 measurements, MM 1 and MM 2 have radial velocities of -4.1 ± 0.3 and -0.7 ± 0.3 km s^{-1}, consistent with the observed maser emission in DR 21 (OH) being of the "shell-type" variety. In this scenario, the maser group at -3.77 km s^{-1} traces a component of a shell which is expanding perpendicular to our line of sight. The maser groups at 10.38 and -10.50 km s^{-1} sample the near (redshifted relative

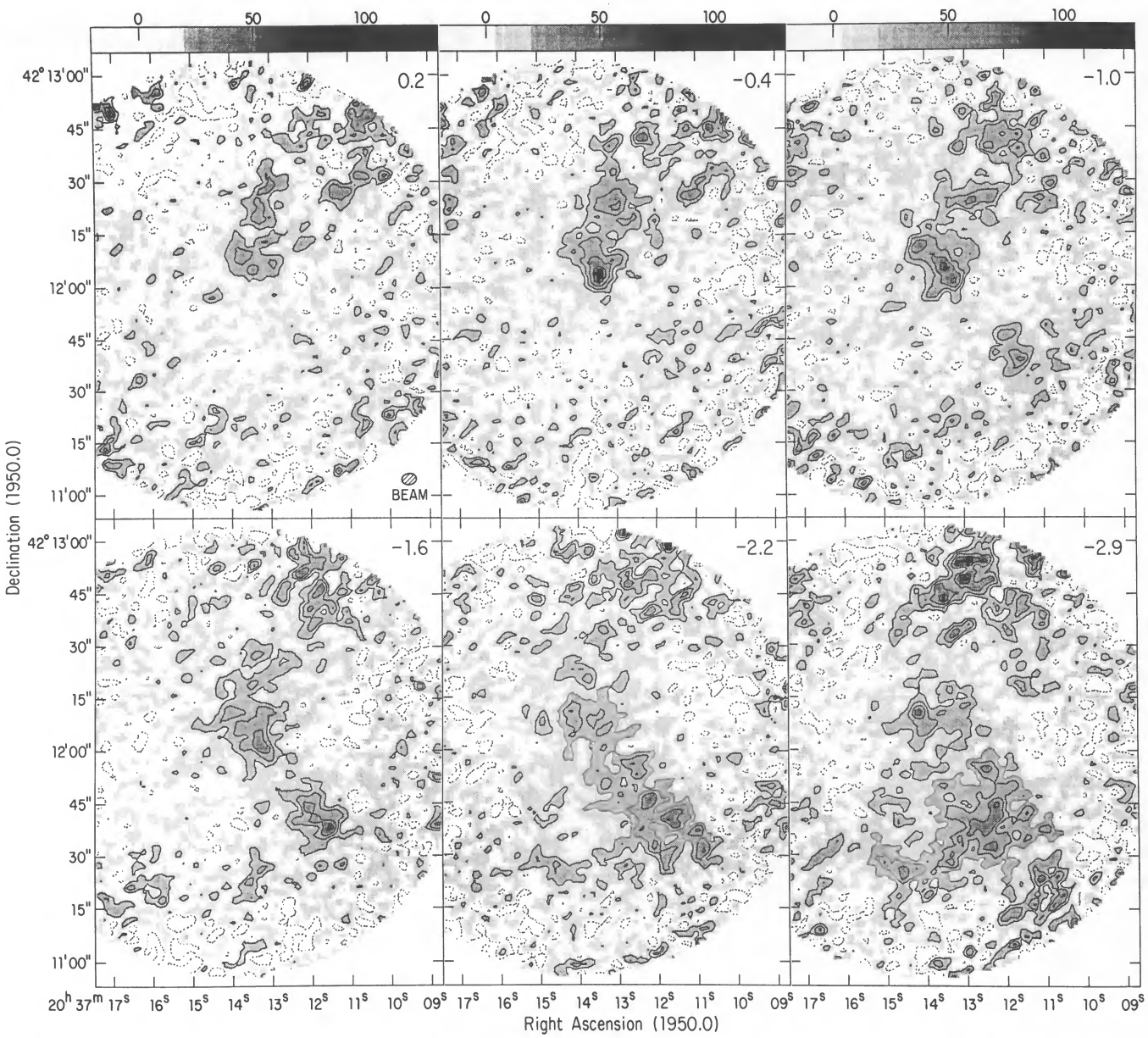

FIG. 2.—$NH_3(2, 2)$ $\Delta F = 0$ emission channel maps toward DR 21 (OH). The contours and the gray scale are the same as in Fig. 1. The LSR velocity with respect to the frequency of the (2, 2) $F = 3 \rightarrow 3$ transition for each channel is indicated.

to MM 2) and far (blueshifted relative to MM 2) sides of an expanding stellar shell associated with MM 2 (see Genzel & Downes 1977) for a pictorial representation of this model).

4. ANALYSIS

4.1. *Global Source Characteristics*

On a spatial scale comparable to the primary beam in these observations (1.'9) the ammonia emission traces a ridge of width $\sim 45''$ (~ 0.7 pc at a distance of 3 kpc) which runs along a position angle of $\sim 15°$ west of north. On larger spatial scales, Wilson & Mauersberger (1990) have mapped the DR 21/DR 21 (OH) region over an area of $3.'3 \times 12.'0$ in the $NH_3(1, 1)$ and (2, 2) transitions. They find that both transitions extend from $\sim 2'$ south to $\sim 4'$ north of the OH maser position, with a breadth of $\sim 2'$ in the east-west direction, centered $\sim 30''$ west of the OH maser position. The position angle of this ridge within $2'$ of the OH maser position is similar to that observed in our high-resolution maps. Therefore, it appears that the structure observed on scales greater than $\sim 2'$ is retained in our observations.

It is apparent from Figure 3 that the NH_3 emission from the $2'$ section of this ridge around the DR 21 (OH) region is composed of four primary components [DR 21 (OH) N, DR 21 (OH) main, DR 21 (OH) W, and DR 21 (OH) S] which are embedded in an overall clumpy medium. Figures 1–3 also show that the NH_3 emission is clumped on scales as small as our synthesized beam ($4''$). To test the reality of these clumpy structures, we have applied the following selection process to our observations:

1. $NH_3(1, 1)$ $\Delta F = 0$ emission features which persisted for at

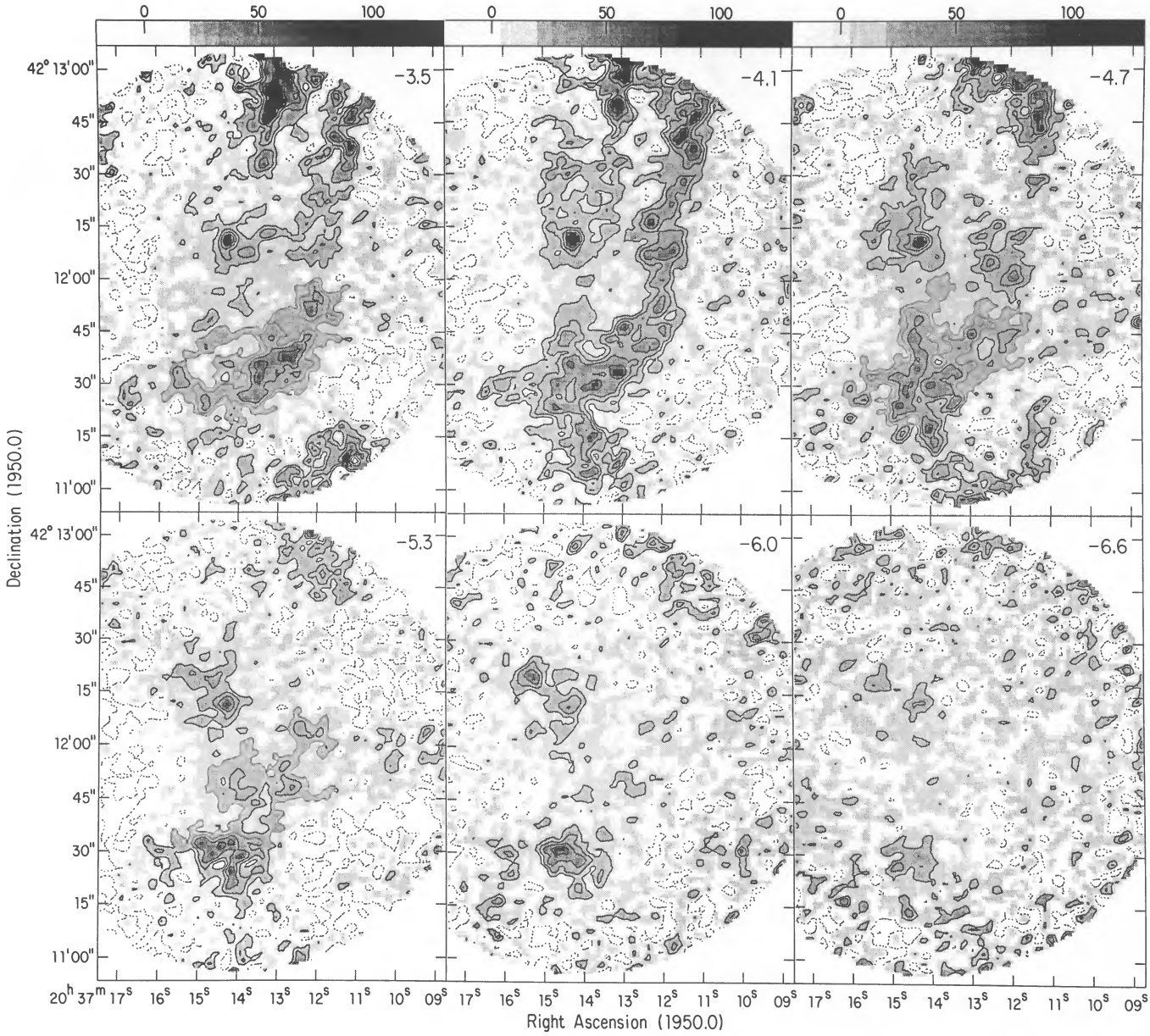

FIG. 2.—*Continued*

least two channels in a given volume of position-velocity space at a level of 3 or more times the individual channel rms noise were identified as candidate cores.

2. Using the (1, 1) $\Delta F = 0$ position and LSR velocity, we searched for corresponding features in our (1, 1) $F = 1 \rightarrow 2$, $F = 1 \rightarrow 0$, and (2, 2) $\Delta F = 0$ maps. Candidate cores identified in at least the (1, 1) $F = 1 \rightarrow 2$ and (2, 2) $\Delta F = 0$ transitions are believed to represent real features in the DR 21 (OH) molecular ridge.

With this conservative selection process we have identified seven individual emission cores within the four "primary" emission components [DR 21 (OH) main and DR 21 (OH) W each contain two subcomponents] and 11 "secondary" emission cores, many of which may be composed of two or more components. Tables 2 and 3 list the position and size (determined by fitting one-component Gaussians to the peak channel map for each source), peak NH_3 hyperfine component brightness temperatures, single-channel rms noise, LSR velocity, and FWZI for each core identified. In Figure 3 we mark the position of each core.

In the following sections, we analyze the detailed physical characteristics of each of the NH_3 emission cores and, within these derived properties, investigate the dynamical state and star-forming properties of the immediate DR 21 (OH) region.

4.2. *Individual* NH_3 *Core Properties*

The high signal-to-noise and spatial resolution afforded by our NH_3 data set allows us to determine the detailed physical properties of each of the DR 21 (OH) NH_3 emission cores. Using an analysis which assumes local thermodynamic equilibrium (LTE; see Appendix), two different methods have been used to calculate the main hyperfine component optical depth,

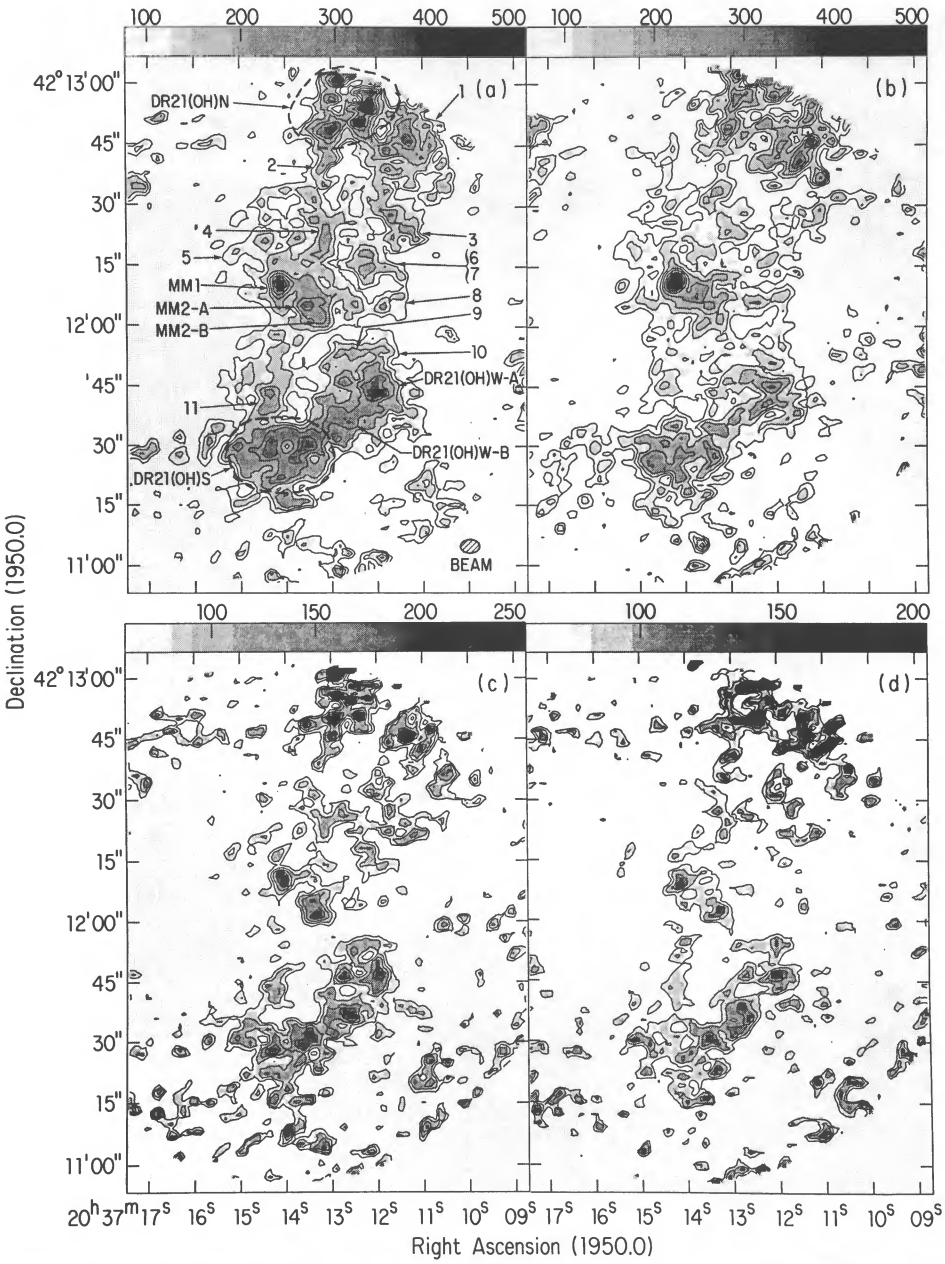

FIG. 3.—NH_3 integrated intensity maps toward DR 21 (OH). (*a*) Integrated (1, 1) $\Delta F = 0$ intensity over the velocity range 1.8 to -6.2 km s^{-1}. The contours are 60, 120, 180, 240, 300, 360, 420, and 480 mJy beam^{-1} km s^{-1} (9.6, 19.2, 28.8, 38.4, 48.0, 57.6, 67.2, and 76.8 K km s^{-1}), while the gray scale runs from 60 to 500 mJy beam^{-1} km s^{-1} (9.6–80 K km s^{-1}). Secondary NH_3 cores 1–11, the primary NH_3 emission components, and the synthesized beam are indicated. (*b*) Integrated (2, 2) $\Delta F = 0$ intensity over the velocity range 2.1 to -6.6 km s^{-1}. The contours are the same as in (*a*). (*c*) Integrated (1, 1) $F = 1 \rightarrow 2$ intensity over the velocity range -6.2 to -13.6 km s^{-1} [V_{LSR} with respect to (1, 1) $F = 2 \rightarrow 2$]. The contours are 60, 100, 140, 180, 220, 260, and 300 mJy beam^{-1} km s^{-1} (9.6, 16.0, 22.4, 28.8, 35.2, 41.6, and 48.0 K km s^{-1}), while the gray scale runs from 60 to 250 mJy beam^{-1} km s^{-1} (9.6–40.0 K km s^{-1}). (*d*) Integrated (1, 1) $F = 1 \rightarrow 0$ intensity over the velocity range -18.6 to -26.0 km s^{-1} [V_{LSR} with respect to (1, 1) $F = 2 \rightarrow 2$]. The contours are 60, 100, 140, 180, and 220 mJy beam^{-1} km s^{-1} (9.6, 16.0, 22.4, 28.8, and 35.2 K km s^{-1}), while the gray scale runs from 60 to 200 mJy beam^{-1} km s^{-1} (9.6–32.0 K km s^{-1}).

$\tau(J, K, m)$, and inversion state column density $N(J, K)$, for each core. An *average* $\tau(J, K, m)$, $N(J, K)$, and $N_{TOT}(NH_3)$ has been measured for each NH_3 core using the following procedure:

1. The velocity extent for each NH_3 core was determined by examination of the (1, 1) and (2, 2) channel maps (Figs. 1 and 2). Velocity integrated emission maps of each hyperfine component in each core were then made by summing the appropriate channel maps.

2. To avoid biasing toward higher integrated intensity in the stronger hyperfine transitions, an integrated spatial NH_3 core size was determined using the (1, 1) $F = 1 \rightarrow 0$ velocity integrated emission map for each core. A spatial integration over the core size was then made to determine the total integrated hyperfine flux from each hyperfine transition toward each core.

3. $\tau(1, 1, m)$ and $\tau(2, 2, m)$ were then calculated for each NH_3 emission core using these integrated hyperfine flux measurements in equations (A2) and (A4). These optical depth measurements are given as the first entry for each core in Tables 4 and 5.

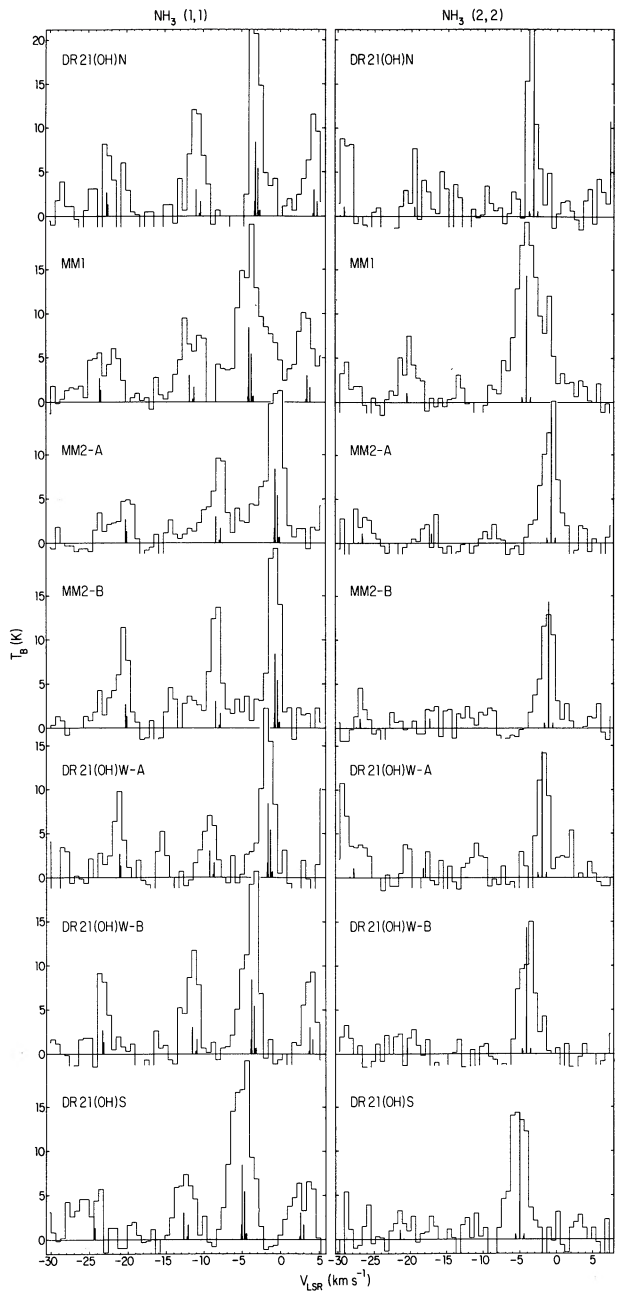

FIG. 4.—Representative spectra through the $NH_3(1, 1)$ $\Delta F = 0$ and (2, 2) $\Delta F = 0$ emission peaks for each of the primary (and associated subcomponent) emission features. Vertical bars mark the positions and relative intensities for the hyperfine components of both transitions. These spectra show the spectral characteristics of each core. Note that because all of the hyperfine components of the (1, 1) transition do not necessarily peak at exactly the same position, these spectra were not used to derive the peak T_B values listed in Table 2.

4. The average $\tau(1, 1, m)$, along with the total integrated (1, 1) $\Delta F = 0$ and (2, 2) $\Delta F = 0$ hyperfine flux measurements, were used in equation (A18) to calculate the excitation temperature for the (1, 1) and (2, 2) transitions, $T_{ex}(2, 2; 1, 1)$.

5. $T_{ex}(2, 2; 1, 1)$, $\tau(1, 1, m)$, and $\tau(2, 2, m)$ from Tables 4 and 5 along with the FWZI from Tables 2 and 3 were then used in equations (A11) and (A12) to calculate the average inversion transition column densities, $N(1, 1)$ and $N(2, 2)$. Equation (A13) was then used to make two independent calculations of the

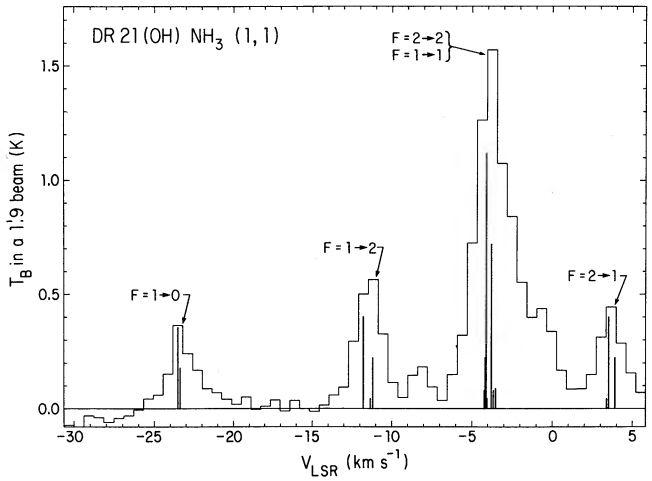

FIG. 5.—Integrated spectrum of the $NH_3(1, 1)$ emission. The integrated emission over the primary beam (1'9) for each channel is plotted to produce this spectrum. Vertical bars mark the positions and relative intensities for the hyperfine components of the (1, 1) transition. The strongest hyperfine component is centered at the central velocity for MM 1 (-4.1 km s^{-1}).

total NH_3 column density $N_{TOT}(NH_3)$ for each core. As with the average optical depth measurements, these average column densities are listed as the first set of entries for each core in Tables 4 and 5.

Peak $\tau(J, K, m)$ and $N(J, K)$ were calculated using the peak brightness temperatures and FWZI's listed in Tables 2 and 3 and $T_{ex}(2, 2; 1, 1)$ from Tables 4 and 5 in equations (A2), (A4), (A11), and (A12). Estimates of the peak $T_{ex}(2, 2; 1, 1)$ did not differ significantly from the average values but did have much larger uncertainties, so we have used our estimates of the average $T_{ex}(2, 2; 1, 1)$ in these calculations. The peak total NH_3 column density was calculated from $N(J, K)$ using equation (A13). These peak values are listed as the second entry for each core in Tables 4 and 5. Note that the uncertainties quoted for $\tau(1, 1, m)$ represent the spread of the independent calculations of $\tau(1, 1, m)$ from the hyperfine components, which is a more realistic estimation of the uncertainty in the measurements than those derived from purely statistical arguments. The

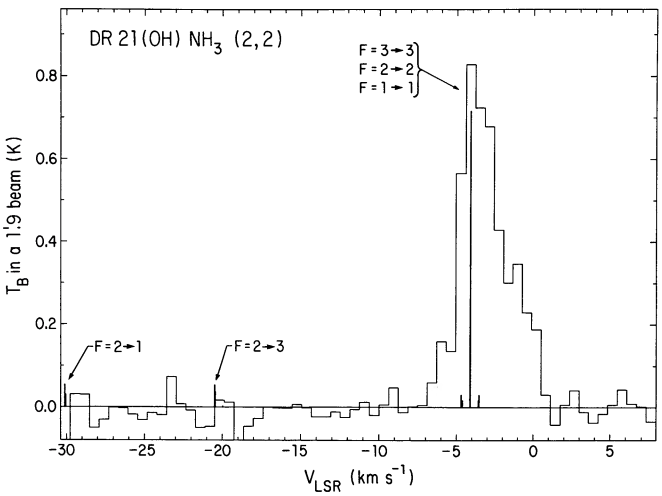

FIG. 6.—Integrated spectrum of the $NH_3(2, 2)$ emission. This figure was produced in the same way as Fig. 5. Vertical bars mark the positions and relative intensities for the hyperfine components of the (2, 2) transition.

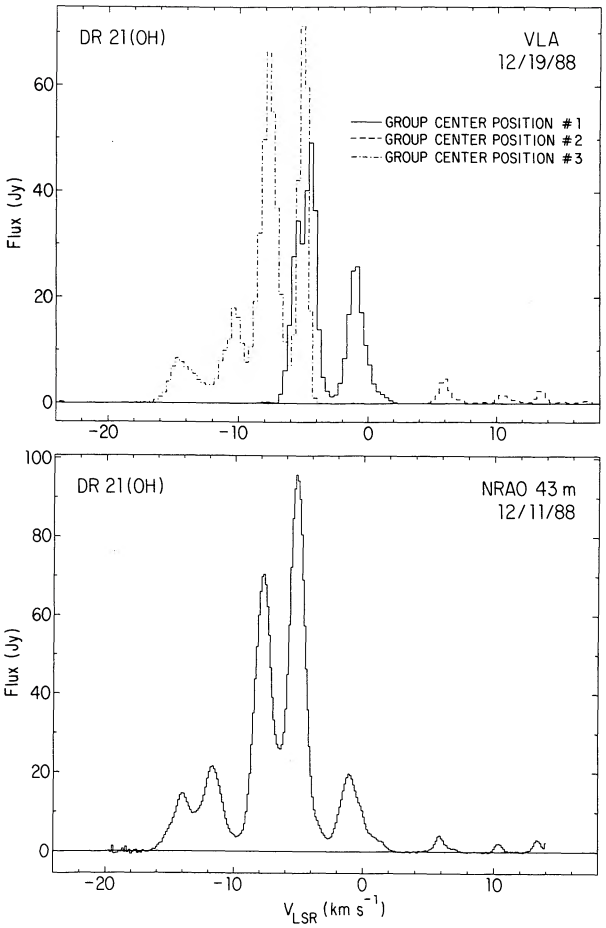

FIG. 7.—Interferometric and single-antenna H_2O maser spectra from DR 21 (OH). The top panel shows the H_2O maser spectrum produced from our VLA A-array observations. The contribution due to each maser component is indicated. The lower panel is a single-antenna spectrum taken with the NRAO 43 m telescope on the date shown in the upper right.

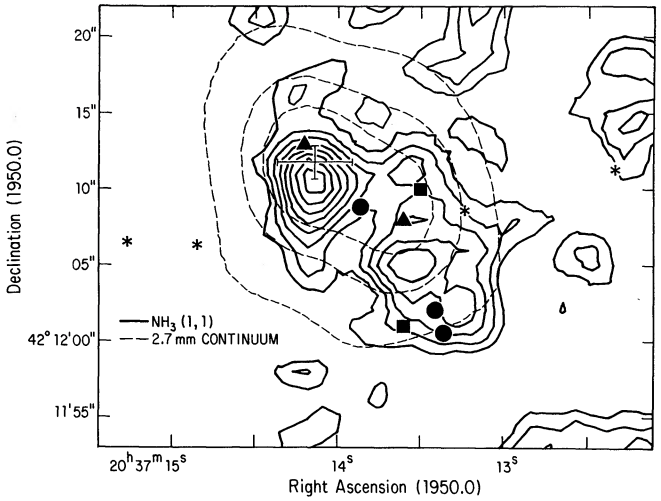

FIG. 8.—Close-up view of the MM 1/MM 2 region. The contour values for the integrated intensity from the $\Delta F = 0$ (main) hyperfine component of the (1, 1) transition are 160, 200, 240, 280, 320, 360, 400, 440, and 480 mJy beam^{-1} km s^{-1} (25.6, 32.0, 38.4, 44.8, 51.2, 57.6, 64.0, 70.4, and 76.8 K km s^{-1}). Shown superposed on the NH_3(1, 1) distribution is the 2.7 mm continuum emission (Paper I). The 2.7 mm continuum contours are 24, 72, and 120 mJy beam^{-1} (6.″9 × 7.″7 beam). Also shown are positions of the 1.4 mm continuum peaks (*filled triangles:* Woody et al. 1989), $2_{11} \rightarrow 2_{12}$ H_2CO emission peaks (*filled squares:* Johnston, Henkel, & Wilson 1984), and OH (*cross:* Norris et al. 1982), CH_3OH (*stars:* Plambeck & Menten 1990), and H_2O (*filled circles:* this work) maser emission peaks. MM 2-B is the component farthest to the southwest, while MM 2-A lies just to the northeast of MM 2-B.

uncertainties quoted for $\tau(2, 2, m)$, $N(1, 1)$ $N(2, 2)$, and $T_{ex}(2, 2; 1, 1)$ are statistical 1 σ values.

A calculation of the gas mass, M_G, has been made for each core using the average NH_3 column density calculated above, assuming that each core is a disk in projection of size $\theta_S = (\theta_{maj}\,\theta_{min})^{1/2}$ with $X(NH_3) = 10^{-8}$ (Batrla et al. 1983; Wilson & Mauersberger 1990). Finally, we have calculated the kinetic temperature T_K, for each source by solving equation (A20)

TABLE 1

H_2O MASER COMPONENT CHARACTERISTICS

Mean Position[a] (10^{-3} arcsec) (1)	$\theta_{max} \times \theta_{min}$[b] ($10^{-3}$ arcsec) (2)	Central Velocity (km s^{-1}) (3)	FWZI (km s^{-1}) (4)	Peak Flux (Jy) (5)	Comments (6)
Group Center Position 1 ($20^h37^m13^s.8620$, 42°12′08.″843)					
(4.3, −7.9)	6.8 × 1.3	−1.03	4.93	25.84	Possible double
(11.6, −17.9)	4.5 × 2.7	−4.64	2.96	49.24	Blend
(−6.2, 7.1)	1.3 × 0.6	−5.63	3.29	34.50	Blend
Group Center Position 2 ($20^h37^m13^s.4084$, 42°12′02.″042)					
(0.5, −1.9)	4.3 × 2.6	5.88	2.63	4.71	
(−40.6, −11.2)	6.9 × 4.3	6.87	1.64	0.75	
(−51.5, −20.5)	8.4 × 3.7	10.16	2.63	1.66	Possible double
(−56.1, −15.0)	3.7 × 3.6	13.12	2.30	2.43	
(−28.5, −41.8)	6.4 × 4.7	15.85	3.29	0.13	Possible double
Group Center Position 3 ($20^h37^m13^s.3629$, 42°12′00.″467)					
(−3.6, 5.3)	4.1 × 1.9	−14.84	4.28	8.51	Possible triple
(−10.0, 12.1)	4.6 × 1.8	−13.86	3.29	6.22	Possible triple
(−12.5, 14.8)	3.2 × 1.0	−10.57	4.61	18.00	
(−9.0, 9.7)	3.1 × 3.1	−7.93	5.59	66.62	
(−1.8, 0.8)	4.9 × 3.8	−5.30	2.30	71.31	

[a] Relative to field center position in (α, δ).
[b] Maximum and minimum angular size for each group.

TABLE 2

PRIMARY NH_3 CORE PROPERTIES

Component (1)	Transition (2)	α(1950) (3)	δ(1950) (4)	$\theta_{maj} \times \theta_{min}$ (arcsec) (5)	Peak T_B[a,b] (K) (6)	rms[b] (K) (7)	V_{LSR}[c] (km s^{-1}) (8)	FWZI[c] (km s^{-1}) (9)
DR 21 (OH) N	(1, 1)	$20^h37^m13^s.0$	42°12′55″	21.2 × 8.0	24.0/11.0/7.0	3.2	−3.2	4.3
	(2, 2)	20 37 13.0	42 12 53	19.6 × 9.5	21.7	3.2	−3.2	3.7
MM 1	(1, 1)	20 37 14.2	42 12 11	5.6 × 4.1	20.0/9.9/7.4	1.6	−4.1	6.8
	(2, 2)	20 37 14.2	42 12 11	6.6 × 4.7	20.9/7.7[d]	1.6	−4.1	8.6
MM 2-A	(1, 1)	20 37 13.5	42 12 06	11.5 × 7.2	17.5/10.2/9.0	1.6	−0.7	3.7
	(2, 2)	20 37 13.5	42 12 05	10.6 × 7.2	17.0	1.6	−0.7	2.5
MM 2-B	(1, 1)	20 37 13.4	42 12 03	9.2 × 6.9	20.6/13.9/11.4	1.6	−0.7	2.5
	(2, 2)	20 37 13.4	42 12 03	12.5 × 7.8	13.6	1.6	−1.0	2.5
DR 21 (OH) W-A	(1, 1)	20 37 11.9	42 11 42	19.8 × 10.4	19.2/7.1/5.0	1.9	−1.6	3.7
	(2, 2)	20 37 11.8	42 11 40	18.1 × 8.9	14.2	1.9	−1.9	3.1
DR 21 (OH) W-B	(1, 1)	20 37 13.0	42 11 36	25.5 × 12.6	20.5/15.6/9.7	1.8	−3.7	3.7
	(2, 2)	20 37 13.1	42 11 35	31.2 × 12.6	15.0	1.8	−4.1	3.1
DR 21 (OH) S	(1, 1)	20 37 14.2	42 11 34	19.6 × 12.6	20.5/7.4/5.8	1.8	−5.0	4.9
	(2, 2)	20 37 14.2	42 11 30	18.2 × 8.3	14.5	1.9	−5.0	4.9

[a] For the (1, 1) transition, brightness temperatures for each hyperfine transition are given as $\Delta F = 0/F = 1 \rightarrow 2/F = 1 \rightarrow 0$.
[b] Measurements include corrections due to the response of the primary beam.
[c] Error in measurement typically one-half of a channel width, or 0.3 km s^{-1}.
[d] Two hyperfine transitions in the (2, 2) transition were detected toward this component, given as $\Delta F = 0/F = 2 \rightarrow 3$.

TABLE 3

SECONDARY NH_3 CORE PROPERTIES

Core (1)	Transition (2)	α(1950) (3)	δ(1950) (4)	$\theta_{maj} \times \theta_{min}$ (arcsec) (5)	Peak T_B[a,b] (K) (6)	rms[b] (K) (7)	V_{LSR}[c] (km s^{-1}) (8)	FWZI[c] (km s^{-1}) (9)
1.....	(1, 1)	$20^h37^m11^s.3$	42°12′45″	14.0 × 8.9	23.9/26.5/17.5	3.1	−4.1	2.5
	(2, 2)	20 37 11.2	42 12 46	16.4 × 5.7	15.6	3.3	−4.1	2.5
2.....	(1, 1)	20 37 13.2	42 12 42	10.5 × 0.9	15.7/12.9/...	2.5	−0.3	1.2
	(2, 2)	20 37 13.2	42 12 41	9.2 × 3.5	10.3	2.5	−0.7	1.2
3.....	(1, 1)	20 37 11.3	42 12 26	9.5 × 5.5	11.5/10.2/8.0	2.2	0.3	2.5
	(2, 2)	20 37 11.1	42 12 28	11.5 × 4.4	9.8	2.2	−0.1	2.5
4.....	(1, 1)	20 37 13.1	42 12 22	13.9 × 9.5	18.5/9.9/5.0	1.8	−0.1	3.7
	(2, 2)	20 37 13.1	42 12 23	15.2 × 12.2	11.3	1.8	−0.1	2.5
5.....	(1, 1)	20 37 15.4	42 12 19	10.4 × 5.4	15.3/7.7/5.6	1.8	−5.6	1.2
	(2, 2)	20 37 15.3	42 12 19	7.7 × 6.2	13.3	1.8	−6.0	1.9
6.....	(1, 1)	20 37 12.1	42 12 18	13.9 × 6.5	18.4/13.8/4.2	1.9	−4.1	2.5
	(2, 2)	20 37 12.1	42 12 17	14.6 × 7.5	14.8	1.9	−4.1	1.9
7.....	(1, 1)	20 37 12.3	42 12 15	8.6 × 4.7	14.6/4.4/...	1.8	−0.1	1.9
	(2, 2)	20 37 12.2	42 12 13	8.0 × 4.0	6.3	1.8	−0.1	1.2
8.....	(1, 1)	20 37 11.8	42 12 09	14.5 × 9.6	18.7/11.1/4.2	1.8	−4.7	2.5
	(2, 2)	20 37 11.9	42 12 08	13.8 × 10.4	13.7	1.8	−4.4	2.5
9.....	(1, 1)	20 37 12.6	42 11 54	7.3 × 4.7	15.2/8.5/6.3	1.7	−2.2	1.9
	(2, 2)	20 37 12.5	42 11 54	7.8 × 4.8	11.9	1.7	−2.6	1.2
10.....	(1, 1)	20 37 12.0	42 11 52	13.2 × 9.1	17.3/10.7/10.5	1.8	−3.4	1.2
	(2, 2)	20 37 12.0	42 11 52	10.7 × 8.4	12.9	1.8	−3.8	1.2
11.....	(1, 1)	20 37 14.3	42 11 42	13.2 × 11.5	18.6/9.0/8.5	1.7	−4.4	4.3
	(2, 2)	20 37 14.3	42 11 43	13.8 × 5.5	13.3	1.7	−4.4	4.3

[a] For the (1, 1) transition, brightness temperatures for each hyperfine transition are given as $\Delta F = 0/F = 1 \rightarrow 2/F = 1 \rightarrow 0$.
[b] Measurements include corrections due to the response of the primary beam.
[c] Error in measurement typically one-half of a channel width, or 0.3 km s^{-1}.

TABLE 4

PRIMARY NH_3 CORE OPTICAL DEPTH, EXCITATION TEMPERATURE, AND COLUMN DENSITY

Component[a] (1)	$\tau(1, 1, m)$ (2)	$N(1, 1)^b$ (10^{15} cm^{-2}) (3)	$\tau(2, 2, m)$ (4)	$N(2, 2)^b$ (10^{15} cm^{-2}) (5)	$T_{ex}(2, 2; 1, 1)$ (K) (6)	$N_{TOT}(NH_3)^c$ (10^{15} cm^{-2}) (7)
DR 21 (OH) N	1.4 ± 0.4	1.9 ± 0.7	0.8 ± 0.1	0.4 ± 0.1	22.7 ± 4.0	11.4
	1.2 ± 0.5	2.1 ± 1.3	1.0 ± 0.5	0.7 ± 0.5	...	15.7
MM 1	$\ll 1$	1.9 ± 0.2	$\ll 1$	1.2 ± 0.1	40.0 ± 0.1	17.9
	1.8 ± 0.2	6.3 ± 2.4	7.7 ± 2.2^d	17.4 ± 5.1	...	161.8
MM 2-A	1.8 ± 0.2	...	1.1 ± 0.1	...	23.1 ± 1.8	...
	2.9 ± 0.1	3.9 ± 1.3	2.1 ± 0.9	0.9 ± 0.5	...	24.0
MM 2-B	1.8 ± 0.2	2.2 ± 0.5^e	1.1 ± 0.1	0.6 ± 0.1^e	23.1 ± 1.8	14.7[e]
	3.7 ± 0.2	2.1 ± 0.6	1.0 ± 0.3	0.3 ± 0.1	...	10.7
DR 21 (OH) W-A	1.2 ± 0.1	1.2 ± 0.2	0.5 ± 0.1	0.2 ± 0.04	19.9 ± 1.0	7.2
	0.7 ± 0.2	0.9 ± 0.4	0.5 ± 0.2	0.2 ± 0.1	...	6.2
DR 21 (OH) W-B	1.3 ± 0.3	1.3 ± 0.4	0.6 ± 0.1	0.2 ± 0.06	19.5 ± 2.3	7.7
	3.8 ± 1.3	3.4 ± 1.5	1.3 ± 0.4	0.4 ± 0.2	...	18.0
DR 21 (OH) S	1.0 ± 0.1	1.6 ± 0.3	0.6 ± 0.1	0.4 ± 0.1	23.5 ± 2.1	9.6
	0.7 ± 0.1	1.2 ± 0.3	0.4 ± 0.1	0.3 ± 0.1	...	7.3

[a] For each component, the first row gives *average* values, while the second row gives *peak* values for $\tau_m(J, K)$ and $N(J, K)$.
[b] For $\tau_m \ll 1$, peak T_B for the main hyperfine transition and FWZI from Table 2 have been used to calculate N.
[c] Average from calculations using $N(1, 1)$ and $N(2, 2)$.
[d] Peak $\tau(2, 2, m)$ calculated using (2, 2) hyperfine intensities.
[e] Sum of components MM 2-A and MM 2-B.

TABLE 5

SECONDARY NH_3 CORE OPTICAL DEPTH, EXCITATION TEMPERATURE, AND COLUMN DENSITY

Component[a] (1)	$\tau(1, 1, m)$ (2)	$N(1, 1)^b$ (10^{15} cm^{-2}) (3)	$\tau(2, 2, m)$ (4)	$N(2, 2)^b$ (10^{15} cm^{-2}) (5)	$T_{ex}(2, 2; 1, 1)$ (K) (6)	$N_{TOT}(NH_3)^c$ (10^{15} cm^{-2}) (7)
1	2.8 ± 0.7	1.8 ± 0.7	1.1 ± 0.1	0.3 ± 0.1	18.5 ± 2.2	11.6
	>4.0	>2.8	>1.0	>0.4	...	16.8
2	1.2 ± 1.4	0.3 ± 0.5	0.4 ± 0.3	0.05 ± 0.05	17.6 ± 10.9	2.4
	~ 6.0	~ 1.4	~ 1.0	~ 0.1	...	6.8
3	$\ll 1$	0.4 ± 0.1	$\ll 1$	0.2 ± 0.05	21.8 ± 0.2	4.1
	6.6 ± 1.3	3.8 ± 1.8	1.9 ± 1.7	0.5 ± 0.4	...	19.7
4	1.4 ± 0.7	1.6 ± 1.0	0.8 ± 0.3	0.3 ± 0.2	22.8 ± 8.2	9.3
	1.5 ± 0.9	1.5 ± 1.1	0.6 ± 0.3	0.2 ± 0.1	...	7
5	1.4 ± 0.4	0.8 ± 0.5	1.4 ± 0.3	0.5 ± 0.3	31.8 ± 8.7	7.5
	1.8 ± 0.3	0.8 ± 0.5	1.3 ± 0.5	0.4 ± 0.2	...	6.6
6	1.2 ± 0.4	0.7 ± 0.3	0.4 ± 0.1	0.1 ± 0.03	17.2 ± 2.5	4.4
	2.5 ± 2.4	1.9 ± 2.2	1.3 ± 0.8	0.4 ± 0.3	...	15.0
7	<0.5	<0.6	<0.2	<0.05	~ 20	<2.8
	~ 0.2	~ 0.1	~ 0.1	~ 0.01	...	~ 0.5
8	<0.8	<0.8	<0.4	<0.2	~ 21	<5.4
	1.5 ± 1.5	1.2 ± 1.4	0.8 ± 0.6	0.3 ± 0.3	...	8.3
9	2.5 ± 1.8	1.1 ± 0.9	0.8 ± 0.2	0.1 ± 0.06	17.1 ± 5.3	5.9
	2.3 ± 0.3	1.3 ± 0.5	1.2 ± 0.4	0.2 ± 0.1	...	8.8
10	1.7 ± 0.2	0.6 ± 0.3	0.7 ± 0.1	0.1 ± 0.05	19.2 ± 1.5	3.7
	3.7 ± 0.4	1.1 ± 0.6	1.3 ± 0.5	0.2 ± 0.1	...	7.0
11	0.5 ± 0.2	0.7 ± 0.4	0.3 ± 0.1	0.2 ± 0.1	23.4 ± 7.7	4.8
	2.2 ± 0.3	2.7 ± 0.7	1.0 ± 0.3	0.6 ± 0.2	...	16.4

[a] For each component, the first row gives *average* values, while the second row gives *peak* values for $\tau_m(J, K)$ and $N(J, K)$.
[b] For $\tau_m \ll 1$, peak T_B for the main hyperfine transition and FWZI from Table 2 have been used to calculate N.
[c] Average of calculations using $N(1, 1)$ and $N(2, 2)$.

using the appropriate $T_{ex}(2, 2; 1, 1)$ and collisional excitation rates (from Danby et al. 1988).

4.2.1. *DR 21* (OH) *N*

Located near the northwestern edge of the primary beam in our NH_3 observations, DR 21 (OH) N has only been detected previously in 800 and 1100 μm dust continuum emission (Richardson, Sandell, & Krisciunas 1989), where it is the weakest source in the region. Because this object is located near the half-power radius of the primary beam, the primary beam correction factor is ~ 2. Therefore, one should keep in mind that our determinations of the physical parameters for this source have been subject to large correction factors. Even though we have calculated the physical properties assuming DR 21 (OH) N is one component, Figures 1, 2, and 3 seem to indicate that there may be five or more individual structures in this region. We have made no attempts at deconvolving these structures because of the location of DR 21 (OH) N near the primary-beam half-power radius of these observations.

4.2.2. *DR 21* (OH) *Main*

4.2.2.1. MM 1

Located near the OH maser position MM 1 is a strong source of far-infrared (Harvey et al. 1986), submillimeter (Gear et al. 1988; Richardson et al. 1989), and millimeter (Woody et al. 1989; Paper I) continuum emission. As shown in Figure 8, MM 1 is also associated with H_2O (§ 3.2) and CH_3OH (Plambeck & Menten 1990) masers and $2_{11} \rightarrow 2_{12}$ H_2CO (Johnston, Henkel, & Wilson 1984) emission. In Paper I we pointed out that MM 1 coincides with the southwestern component of a 20 μm continuum emission double source (Genzel 1989) and identified it as the embedded heating source for the dust. The northeastern component of the 20 μm double source has no observed molecular spectral line or millimeter/submillimeter dust continuum emission, suggesting that this object has emerged from the molecular cloud in which it formed. By analyzing the far-infrared to millimeter dust emission spectrum, in Paper I we found that MM 1 appears to contain one or more massive pre–main-sequence star(s). The derived bolometric luminosity for MM 1 is 1.7×10^4 $L_\odot$, which corresponds to a B0.5 V zero-age main-sequence star (Panagia 1973). The detection of H_2O maser "shell-type" emission near this source (see § 3.2) is consistent with this interpretation.

Note that in MM 1, unlike the other NH_3 cores in DR 21 (OH), we have detected the $F = 2 \rightarrow 3$ hyperfine of the (2, 2) inversion transition, indicating much higher column density and/or temperature toward MM 1 when compared to the other DR 21 (OH) NH_3 cores. Note also that MM 1 has the largest FWZI of all the NH_3 cores in the region and that the (2, 2) transition is $\sim 20\%$ broader than the (1, 1) transition.

Unlike the other NH_3 cores in the DR 21 (OH) region, the (1, 1) and (2, 2) transitions toward MM 1 appear, on average, to be optically thin. Also, the peak optical depths, calculated using equation (A2), are 1.8 ± 0.2 and 7.7 ± 2.2, respectively, which implies that $\tau^{peak}(2, 2, m) \simeq 4\tau^{peak}(1, 1, m)$. Use of equation (A8) tells us that the total optical depth on the (2, 2) transition, summed over all hyperfine components, is approximately twice that in the (1, 1) transition. This difference can be caused by several effects:

1. *The beam filling factors for the main and satellite hyperfine transitions are not equal.* By making Gaussian fits to the peak channel of each hyperfine transition toward MM 1, we find that the beam filling factors are ~ 0.6 for all three (1, 1) hyperfine components and that the (2, 2) $\Delta F = 0$ transition has a beam filling factor 40% larger than the (2, 2) $F = 2 \rightarrow 3$ transition. Taking this into account in equation (A2), though, will only widen the difference between the (1, 1) and (2, 2) optical depths. We attribute the lower apparent beam filling factor for the (2, 2) $F = 2 \rightarrow 3$ transition to low signal to noise.

2. *The excitation temperatures in the hyperfine satellites of the* (1, 1) *and* (2, 2) *transitions are not equal to that in the main hyperfine of each transition.* Since the energy separations between the satellite and main hyperfine components of the (1, 1) and (2, 2) transitions are small (< 0.1 K), a difference in excitation temperature is unlikely.

3. *The* (1, 1) *and* (2, 2) NH_3 *emitting regions are not cospatial.* We consider this to be the most likely explanation for the observations. Since MM 1 appears to be a deeply embedded protostar or cluster of young stars (Paper I), a simple model for this source would involve increasing temperatures and densities at smaller radii. Therefore, it is quite possible that the $NH_3(2, 2)$ emission is tracing a denser, warmer, more turbulent component of MM 1 which is closer to the central heating source. If the spatial density is proportional to r^{-2}, then τ will increase at least as fast as the molecular column density, which would be proportional to r^{-1}. Therefore, the larger observed line width and optical depth for the (2, 2) transition could be taken as support for this model. However, the width of a saturated spectral line increases as $[\ln(\tau_{peak})]^{1/2}$ (Phillips et al. 1979), hence opacity broadening could cause the larger line width in the (2, 2) transition.

Table 6 lists our derived source size, temperature, and mass for MM 1. We also include for comparison in Table 6 the source size, dust temperature, and dust mass derived from $C^{18}O$ and millimeter continuum observations (Paper I). Note that because $T_{ex}(2, 2; 1, 1) > 35$ K, only a lower limit to T_K can be calculated (Walmsley & Ungerechts 1983). Given the existence of emission from the (7, 7) transition of NH_3 toward DR 21 (OH) (Mauersberger et al. 1986), which is 535 K above the ground state, it is likely that $T_K > 100$ K in MM 1.

By analyzing the velocity structure of MM 1 as a function of position in the (1, 1) and (2, 2) transitions, we have detected a velocity shift along a position angle of 90°. Figure 9 shows this velocity shift, where we have averaged over declination 42°12′05″ to 42°12′18″ and plotted LSR velocity as a function of right ascension in the (1, 1) $\Delta F = 0$, $F = 1 \rightarrow 2$, $F = 1 \rightarrow 0$, and (2, 2) $\Delta F = 0$ transitions. Note that the strongest components of the magnetic hyperfine structure within the (1, 1) transitions have separations of 0.32, 0.58, and 0.14 km s^{-1}, respectively, displacements much smaller in magnitude than the observed velocity shift. The observed pattern must be caused by source motion, not intensity irregularities within the hyperfine structure. The shift measures ~ 3 km s^{-1} in velocity and $\sim 2''$ in right ascension in all four hyperfine transitions. Rotation, infall, or outflow of the gas could explain this velocity shift.

The existence of CH_3OH maser emission to the east and west of MM 1 may indicate the presence of outflow motions in the region. Plambeck & Menten (1990) have mapped the 98 GHz $8_0 \rightarrow 7_1$ A^+ transition of CH_3OH toward DR 21 (OH) and have detected maser emission at the positions shown in Figure 8. Plambeck & Menten suggest that the CH_3OH masers may be tracing an interface region between a shock and the surrounding ambient material. This interpretation and the

TABLE 6

NH_3 CORE SIZES, TEMPERATURES, AND MASSES

	θ_S[a]								
	Dust		$C^{18}O$						
COMPONENT (1)	1.4 mm (arcsec) (2)	2.7 mm (arcsec) (3)	1.4 mm (arcsec) (4)	2.7 mm (arcsec) (5)	NH_3 (arcsec) (6)	T_D (K) (7)	T_K[b] (K) (8)	M_D ($M_\odot$) (9)	M_G[c] ($M_\odot$) (10)
Primary Cores									
DR 21 (OH) N	...	...	...	...	13	...	32	...	695
MM 1	4	7	10	8	5	58	>80	350	162
MM 2[d]	4	7	10	9	9	30	32	570	430
DR 21 (OH) W-A	...	~9	...	~15	14	≳20	26	≲250	509
DR 21 (OH) W-B	...	...	...	...	19	...	25	...	1003
DR 21 (OH) S	...	15	...	14	15	≳20	33	≲810	780
Secondary Cores									
1	...	...	...	...	10	...	23	...	419
2	...	...	...	...	4	...	~20	...	14
3	...	...	...	...	7	...	30	...	72
4	...	...	...	...	13	...	32	...	567
5	...	...	...	...	7	...	56	...	133
6	...	...	...	...	10	...	21	...	159
7	...	...	...	...	6	...	~25	...	<36
8	...	...	...	...	12	...	~30	...	<281
9	...	...	...	...	6	...	21	...	77
10	...	...	...	...	10	...	25	...	133
11	...	...	...	...	11	...	33	...	210

[a] $\theta_S = (\theta_{maj}\theta_{min})^{1/2}$.

[b] Calculated from $NH_3(1, 1)$ and $NH_3(2, 2)$ rotation temperatures.

[c] Calculated using source size from col. (6), *average* $N_{TOT}(NH_3)$ from col. (7) of Table 4, and assuming $X(NH_3) = 10^{-8}$ (Batrla et al. 1983; Wilson & Mauersberger 1990).

[d] Combination of NH_3 components MM 2-A and MM 2-B.

observed east-west position angle of the CH_3OH masers is consistent with the east-west velocity shift of the NH_3 emission toward MM 1.

The $2_{11} \rightarrow 2_{12}$ H_2CO emission observed toward this source (see Fig. 8) is also displaced from the major NH_3, $C^{18}O$, and dust continuum emission sources. Since $n(H_2) \gtrsim 10^5$ cm^{-3} are required to excite $2_{11} \rightarrow 2_{12}$ H_2CO emission, it is surprising that these emission peaks do not overlap with the dense structures observed using other molecular tracers. Molecular abundance irregularities are not uncommon (Orion-KL and TMC-1, for example, show spatial abundance irregularities). Therefore, NH_3 and H_2CO may be tracing different components of the MM 1/MM 2 region. Alternatively, one can envision a situation where a core/halo density structure exists in DR 21 (OH). In this scenario a dense core emits $2_{11} \rightarrow 2_{12}$ H_2CO emission, but the lower density halo structure produces H_2CO absorption. Perhaps the $2_{11} \rightarrow 2_{12}$ emission in DR 21 (OH) is a region where a hole in the halo allows us to see directly into the dense core.

4.2.2.2. MM 2

MM 2 was originally identified in 1.4 mm continuum (Woody et al. 1989) and $J = 2 \rightarrow 1$ $C^{18}O$ (Padin et al. 1989) maps of DR 21 (OH). It is located ~8″ southwest of MM 1. Observations of the 2.7 mm continuum and $J = 1 \rightarrow 0$ $C^{18}O$ emission (Paper I) found that MM 2 is a dense [peak $n(H_2) = 6.8 \times 10^7$ cm^{-3}] and massive ($M_D = 480\ M_\odot$) condensation which contains at least one massive early-B type star. Figure 8 shows that we have also detected this condensation in NH_3 emission. The emission is actually composed of two components, which we call MM 2-A and MM 2-B.

Because of the close proximity of MM 2-A and MM 2-B (~4″ in position and ~0.3 km s^{-1} in velocity), we have not attempted to calculate the gas mass for each component. From Tables 2 and 4 we see that MM 2-A and MM 2-B are comparable in size, while the measured peak NH_3 column density for MM 2-A is approximately twice that of MM 2-B. Our $NH_3(1, 1)$ and (2, 2) maps reveal no apparent velocity signatures from MM 2-A or MM 2-B which could be interpreted as rotation. However, the detection of "shell-type" H_2O maser emission from MM 2 (see § 3.2) suggests the presence of one or more embedded young stars.

4.2.3. *DR 21* (OH) *W*

Previously detected as a weak and extended source of 800 and 1100 μm (Richardson et al. 1989) and 2.7 mm (Paper I) continuum emission, DR 21 (OH) W represents the primary NH_3 condensation in the western portion of the DR 21 (OH) molecular ridge. Located ~35″ southwest of MM 1 and southwest of W75 (IRS 1), DR 21 (OH) W is actually composed of at least two components, which we designate DR 21 (OH) W-A and DR 21 (OH) W-B.

As Figure 3 indicates, DR 21 (OH) W-B is as bright in the $NH_3(1, 1)$ transition as MM 1, but encompasses 14 times the area. Even though DR 21 (OH) W-A and W-B do appear to have some internal velocity structure, none of these motions is indicative of rotation or infall. The large mass ($M_G \simeq 1500\ M_\odot$) and low temperature ($T_K \simeq 25$ K) in this region suggest

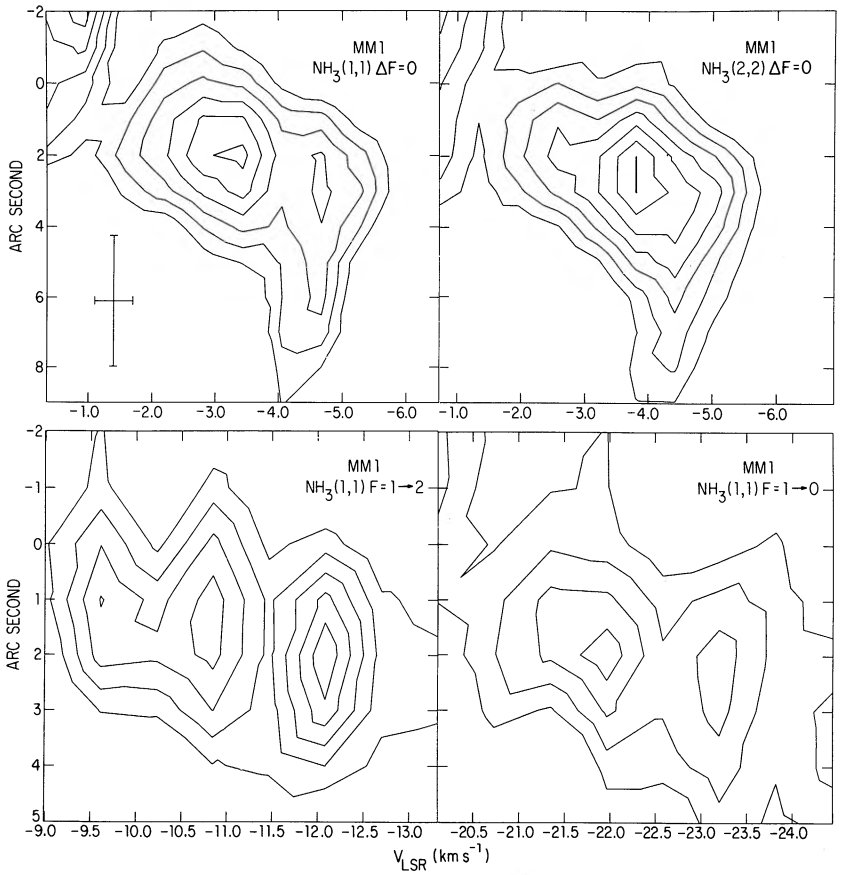

FIG. 9.—V_{LSR}–position diagrams for MM 1. Each diagram was made by averaging over declination 42°12′05″ to 42°12′18″ and ploting V_{LSR} as a function of right ascension (position angle 90°) in each NH_3 hyperfine transition shown. The spatial and spectral resolution is indicated in the first panel. Note that the magnitude and orientation of the velocity shift is the same in all four transitions.

that DR 21 (OH) W is at least a potential star formation site. The analysis presented in Paper I indicates that DR 21 (OH) W harbors at least one massive early-B type star, though the stellar content of this core is not well constrained by existing measurements.

DR 21 (OH) W provides a key element to our understanding of the large-scale structure of the DR 21 (OH) region. The channel maps in Figures 1 and 2 show that as the LSR velocity decreases from 0.9 to -6.5 km s^{-1}, the NH_3 emission shifts from MM 2, through DR 21 (OH) W, and ends at DR 21 (OH) S, forming what appears to be the southern portion of an inclined semishell or evacuated slab of NH_3 emission. In § 5 we will further discuss this interpretation of the large-scale structure of the NH_3 emitting region and its implications regarding the dynamical history of DR 21 (OH).

4.2.4. *DR 21* (OH) *S*

DR 21 (OH) S was first discovered as a strong source of 350 μm continuum emission (Gear et al. 1988). Subsequent high-resolution observations of the 2.7 mm and $C^{18}O$ emission (Paper I) have shown that DR 21 (OH) S has a bolometric luminosity of $\sim 2.5 \times 10^3\ L_\odot$ and a moderate temperature ($T_K \gtrsim 20$ K) and density [$n(H_2) \simeq 10^6$ cm^{-3}]. Since external heating due to cosmic rays, diffuse ultraviolet radiation, and the nearby DR 21 and MM 1/MM 2 sources can supply at most 1% of the observed luminosity, there must be at least one massive early-B star supplying DR 21 (OH) S. Unfortunately, the mid- and far-infrared characteristics of DR 21 (OH) S are as yet unclear.

The structure of the NH_3 emission toward DR 21 (OH) S is, like the nearby source DR 21 (OH) W, quite complex and likely composed of multiple components. Because the DR 21 (OH) S and DR 21 (OH) W-B components are closely associated both in position and velocity, it is difficult to analyze the kinematic properties of the DR 21 (OH) S NH_3 emission. Restricting our analysis to the main emission feature at the DR 21 (OH) S position, we detect no systematic internal velocity structure in this component. It was recognized by Gear et al. (1988) and was apparent in our $J = 1 \rightarrow 0$ $C^{18}O$ and 2.7 mm continuum observations (Paper I), that DR 21 (OH) S is elongated east-west indicating the existence of multiple components. Indeed, we do see two subcomponents in the NH_3(1, 1) and (2, 2) emission toward DR 21 (OH) S (see Fig. 3) located along an east-west position angle.

4.2.5. *Secondary Cores*

As noted in § 3.1, the secondary cores have not been previously detected. On average, the main hyperfine component optical depths and kinetic temperatures for the primary and secondary cores are not significantly different, while the secondary cores are typically $\sim\frac{3}{4}$ of the size and have $\sim\frac{1}{2}$ of the FWZI of the primary cores. This implies that a typical secondary core has $\sim\frac{1}{2}$ of the NH_3 column density and $\sim\frac{1}{3}$ of the mass of a typical primary core. Therefore, the lower sensitivity

and resolution of previous observations have likely hindered the detection of the secondary cores.

As can be derived from the information in Table 3, all but one of the secondary cores have FWZI in the range 1.2–3.7 km s^{-1}. The one exception, core 11, is located just to the north of, and at a similar LSR velocity to, the primary core DR 21 (OH) S, suggesting a dynamical association with this primary core. From Table 6 we find that the secondary cores occupy a large range in M_G, ~15–570 $M_\odot$, and with the exception of core 5, have kinetic temperatures in the range ~20–33 K. Core 5, although its high kinetic temperature of 56 K is rather uncertain [because of a high uncertainty in $T_{ex}(2, 2; 1, 1)$], also distinguishes itself by having a small source size ($\theta_S = 7''$; see Table 6) and FWZI (~1.6 km s^{-1}; see Table 3). Core 5 is located ~17″ to the northeast of MM 1, ~8″ to the northeast of a strong source of 20 μm continuum emission (Genzel 1989; see Paper I), and is slightly blueshifted ($V_{LSR} \simeq -5.8$ km s^{-1}) relative to MM 1 ($V_{LSR} \simeq -4.1$ km s^{-1}). The physical properties derived for core 5 indicate that it likely contains an embedded heat source.

Seven of the 11 secondary NH_3 cores are located along the western edge of the molecular distribution (see Fig. 3). Four of these seven secondary cores form the western edge of an NH_3 ringlike structure at $V_{LSR} \simeq -4$ km s^{-1} (see Fig. 1). The existence of multiple density structures correlated in both position and velocity suggests that a single event led to their formation. We will investigate the physical and dynamical structure of the entire DR 21 (OH) region in § 5.

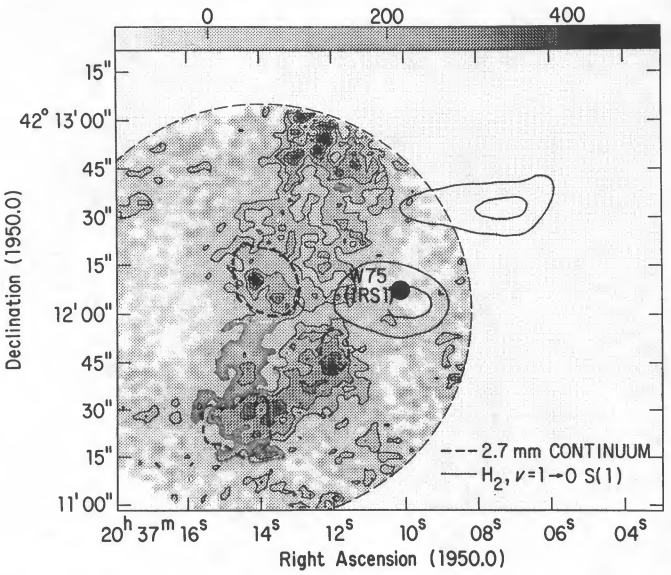

FIG. 10.—Comparison between the NH_3, 2.7 mm continuum, and shocked H_2 emission toward DR 21 (OH). The integrated $NH_3(1, 1)$ $\Delta F = 0$ contours are 120, 180, 240, and 300 mJy $beam^{-1}$ km s^{-1} (19.2, 28.8, 38.4, and 48.0 K km s^{-1}), the 2.7 mm continuum contour is 24 mJy $beam^{-1}$ (3 σ; see Paper I), and the $v = 1 \rightarrow 0$ $S(1)$ H_2 contours are 14 and 21 × 10^{-13} W cm^{-2} sr^{-1} (2 σ and 3 σ; Garden et al. 1986). The circular arc encloses the region where the combined primary-beam response is 40% or more of the peak. A filled circle marks the position of W75 (IRS 1).

5. DISCUSSION

By analyzing the spatial and dynamical structure of the gas in an active star-forming molecular cloud, one can gain information regarding past, present, and future star formation in the region. In the following, we will analyze the available infrared and radio observations of this region in order to develop scenarios which describe the star-cloud interaction in DR 21 (OH). We are forced to develop several scenarios, as opposed to a unified model, primarily because of the lack of information regarding the source of the outflow dynamics and a direct identification of the stellar population in the region.

There are three pieces of observational evidence suggesting that DR 21 (OH) contains a source of mass outflow. Fischer et al. (1985), using 66″ resolution measurements of the CO $J = 1 \rightarrow 0$ transition, discovered the blueshifted wing of a localized, small-scale outflow associated with DR 21 (OH) (the redshifted wing is confused with strong emission from the W75N molecular cloud at $V_{LSR} = 9$ km s^{-1}). Based on their measurements of the size and flux from the blueshifted wing of CO emission, we estimate a mass of ~100 $M_\odot$ for the outflow. Assuming a flow velocity of 15 km s^{-1}, an average core mass of ~300 $M_\odot$, and an average velocity width of ~3 km s^{-1} for the observed NH_3 cores in DR 21 (OH) (see Tables 2, 3, and 6), momentum conservation suggests that this CO outflow can produce the observed NH_3 structures. Unfortunately, though, the relatively low spatial resolution of the CO measurements, lack of high-resolution infrared data, and nondetection of the redshifted wing preclude assignment of this flow to the suspected stellar sources in the region.

The second piece of evidence suggesting the existence of mass outflow in DR 21 (OH) is the detection of the $v = 1 \rightarrow 0$ $S(1)$ transition of shocked H_2 (Garden et al. 1986). A map of the region (see Fig. 10) indicates that the $S(1)$ emission peaks at the position of the strong 2.2 μm infrared source W75 (IRS 1). Unfortunately, the peak signal-to-noise in this measurement is 3:1, making any quantitative analysis of this result difficult. The third and final piece of evidence supporting the mass outflow hypothesis is the detection of broad wings in spectra of the CS $J = 5 \rightarrow 4$ transition toward the MM 1/MM 2 position (Sandell 1990). These broad wings are not seen at the other positions mapped in this source, indicating that the flow may be very localized.

Based on the available dust continuum measurements of DR 21 (OH), there are two primary candidates for the source of the outflow dynamics in the region: W75 (IRS 1) and a source in the MM 1/MM 2 region. In the following we will develop separate (yet similar) concepts which require each of these objects to be the outflow source. We stress that these source concepts are *not* meant to be unified models of the DR 21 (OH) source structure. They are meant to be a proposed framework around which a source model can be constructed.

5.1. *Wind-blown Shell*

Looking at the $NH_3(1, 1)$ and (2, 2) channel maps of Figures 1 and 2 in the velocity range 1.5 to −6.5 km s^{-1} (the main hyperfine components of each transition), the large-scale structure of the emission closely resembles that of an inclined semishell. To clarify this structure, we display in Figure 11 averages over three-channel sections which represent cross sections of this semishell. In this picture, W75 (IRS 1) lies near the center of the semishell.

Thum & Lemke (1975) proposed a model, based on measurements of 1.65–20 μm dust emission, in which W75 (IRS 1) is a dust-embeded young stellar object of ~7 × 10^3 $L_\odot$. Based on 10 μm absorption measurements, Thum & Lemke suggest that the total visual extinction toward W75 (IRS 1) is greater than 25 mag. In our NH_3 observations, W75 (IRS 1) is located in a region where there is no detected emission. Therefore,

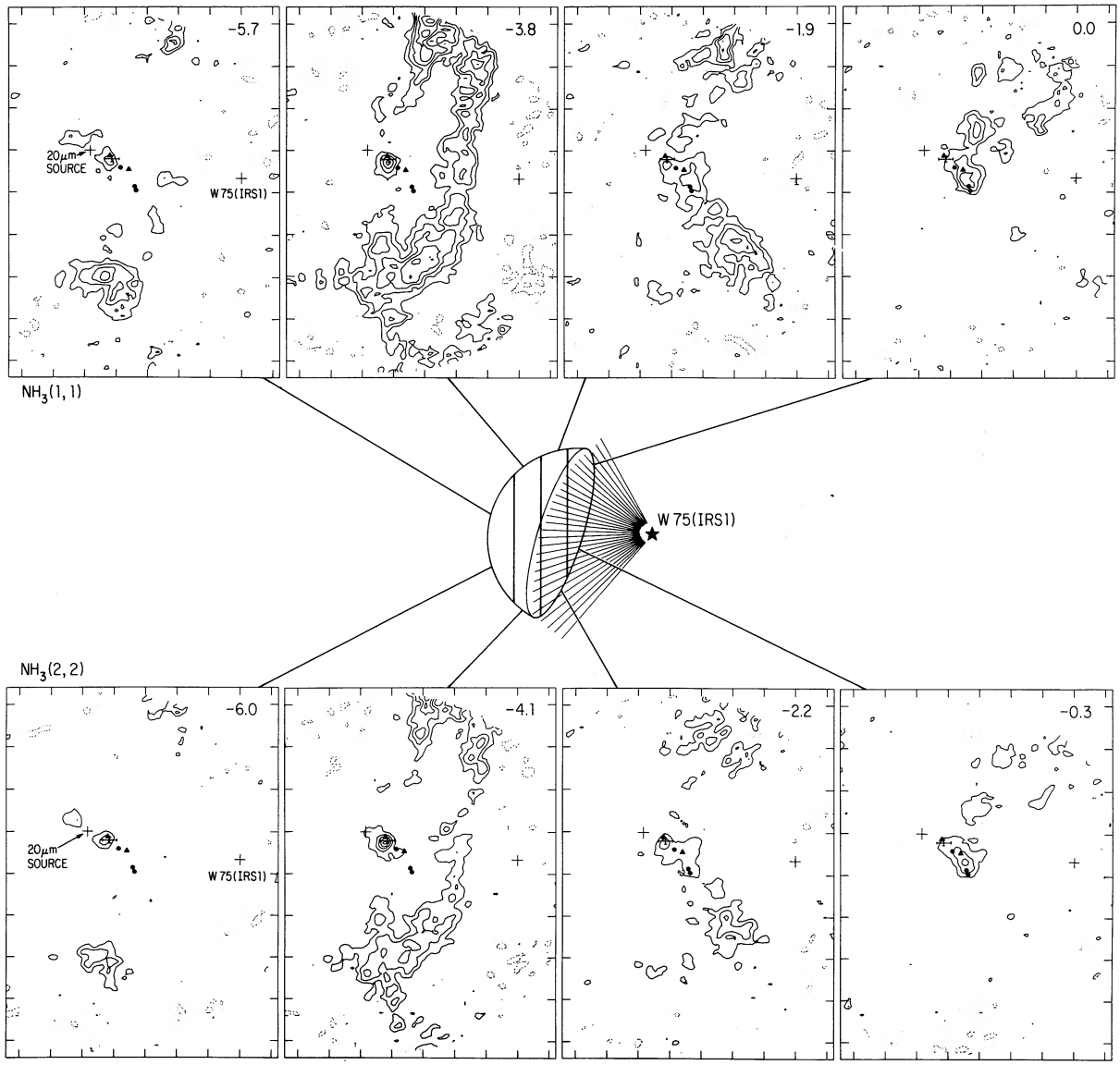

FIG. 11.—Wind-blown shell source concept for DR 21 (OH). Three-channel averages over selected ranges in velocity for the main hyperfine components of the (1, 1) and (2, 2) transitions are shown. The central velocity for each range is indicated in the upper right-hand corner of each plot. NH_3 emission representing each portion of the shell is indicated.

based on the rms noise at the position of W75 (IRS 1) in our spectra of 2.4 K, the spectral channel width of 0.62 km s^{-1}, and assuming an excitation temperature of 15 K, an NH_3 abundance of 10^{-8}, and the standard $N(H_2)$-to-A_v conversion of 0.94×10^{21} cm^{-2} mag^{-1}, we estimate $A_v < 30$ mag, consistent with the infrared measurements.

Young stellar objects produce outflows (Lada 1985; Bally & Lada 1983). Therefore, since W75 (IRS 1) possesses the spectral characteristics of an embedded young stellar object, it is reasonable to suppose that it is the source of the CO outflow described above.

5.2. *Evacuated Slab*

As determined from the far-infrared through millimeter continuum emission properties, the MM 1/MM 2 region contains one or more embedded young B stars (Paper I). It was noted in § 4.2.2 that the MM 1/MM 2 region is composed of two components in 20 μm continuum emission (Genzel 1989) and that we identify MM 1 as the southwestern component of this double source (Paper I). Since MM 1 is a strong NH_3(1, 1) and (2, 2) emission source while the northeastern component of the 20 μm double is devoid of NH_3 emission, MM 1 appears to be the younger object of the two. The evidence for outflow motions from the MM 1/MM 2 region (Fischer et al. 1985; Sandell 1990; see § 5) is not substantial enough for us to be able to make an association with the observed global NH_3 structure. Therefore, given the more evolved state for the northeastern 20 μm companion to MM 1, we suggest that it is a young stellar object similar to W75 (IRS 1). Following the reasoning presented in § 5.1, this northeastern 20 μm source may drive a stellar wind which collides with the dense material in the DR 21 (OH) molecular ridge. In this picture, depicted in Figure 12, the northeastern 20 μm source does not create a cavity in the DR 21 (OH) molecular ridge but rather clears out

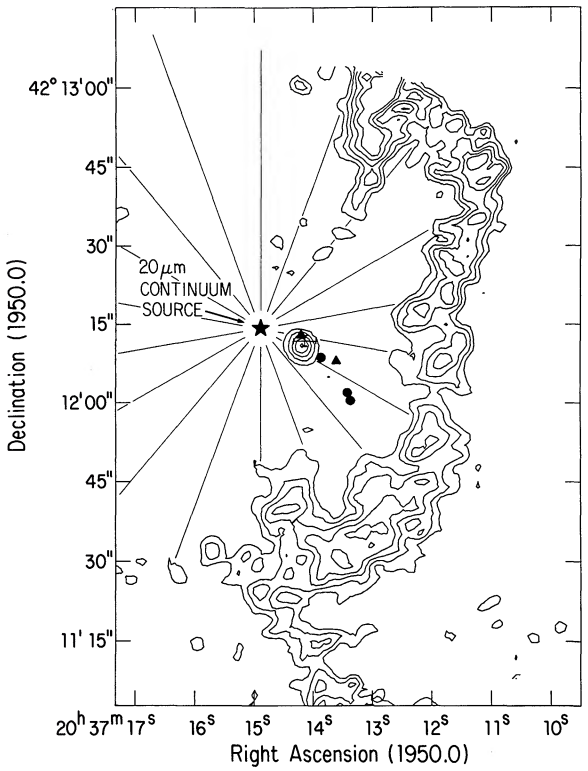

FIG. 12.—Evacuated slab source concept for DR 21 (OH). The $NH_3(1, 1)$ $\Delta F = 0$ channel map at -3.4 km s^{-1} has been used for this representation.

a hole in a slablike section of the ridge. As noted in § 5.1, sensitive centimeter continuum measurements of this region will test this source concept.

5.3. *Source-Concept Synopsis*

Both the wind-blown shell and the evacuated slab concepts are based on the dynamical influences of mass-loss winds from young stellar objects embedded in or near the DR 21 (OH) molecular ridge. Since both of these concepts explain the available observations quite well, it is possible that *both* concepts contribute to produce the observed NH_3 emission distribution. W75 (IRS 1) might be guiding the source structure at larger velocities (-2.8 to 1.5 km s^{-1}), while the northeast 20 μm source might be producing the structures at the lower velocities (-6.5 to -2.8 km s^{-1}). The fact that we cannot favor one concept over the other is due primarily to the lack of an identification of the embedded stellar population in the region.

The dynamical influences of winds and/or outflows from young stars may also play a role in the formation of the large-scale structures ($\theta \geq 2'$) in the DR 21 region. Wilson & Mauersberger (1990) suggest that the column-like shape of the distribution of dense gas in the DR 21 region could be caused by compression by winds from stellar clusters or outflow sources. These young stars are likely distributed in declination at right ascensions east and west of the DR 21 molecular ridge.

The type of NH_3 emission structure observed in DR 21 (OH) has also been detected in other star-forming regions. Torrelles et al. (1989) have detected a shell-like structure around the infrared object AFGL 2591, which they interpret as a cavity produced by a central outflow. Maps of the $NH_3(1, 1)$ and (2, 2) emission toward the Monoceros R2 molecular cloud (Torrelles et al. 1990) show that the NH_3 emission is composed of a collection of condensations which constitute an arclike structure located ~ 0.2 pc from a cometary-like H II region. Massi, Churchwell, & Felli (1988) have detected clumped NH_3 emission located adjacent to an arc-shaped ionization front that separates the diffuse H II region from the molecular cloud in M17. Unlike DR 21 (OH), though, the shell- and arclike structures in AFGL 2591 and M17 do not show the kinematic and spatial detail apparent in Figures 1 and 2. Therefore, with further definition of the infrared and centimeter-wavelength emission characteristics, DR 21 (OH) has the potential to be an excellent site in which to study the interactions between forming stars and their maternal environment.

6. NH_3 CORE MASS STATISTICAL PROPERTIES

In the previous sections we have analyzed the physical and dynamical properties of the NH_3 cores which compose the DR 21 (OH) region. Even though we have identified a relatively small number (18) of cores, we thought it useful to characterize the NH_3 core mass distribution for comparison with other star-forming regions.

6.1. *Mass Spectrum*

Using the NH_3 core masses given in Table 6, we have derived the frequency distribution of core mass, shown in Figure 13*a*. From this the frequency distribution of cores per solar mass interval, (dN/dM), or the "mass spectrum," was calculated (Fig. 13*b*). Assuming that the mass spectrum can be described by a power law of the form $dN/dM \propto M^{-\alpha}$, we have made a least-squares fit of this power law to the data in Figure 13*b*, where we find that $\alpha \simeq 0.7$. Previous determinations of the

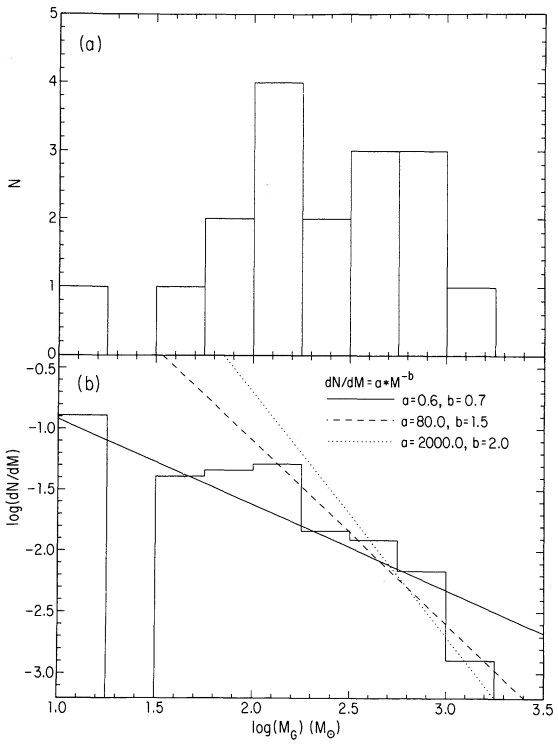

FIG. 13.—NH_3 core mass distribution. In (*a*) we show the frequency distribution of core mass, while (*b*) is a plot of the frequency distribution of core masses per solar mass interval. In (*b*) we also show several representative core mass power laws.

slope of the mass spectrum toward other molecular cloud complexes (Casoli, Combes, & Gérin 1984; Sanders, Scoville, & Solomon 1985; Blitz 1987; Loren 1989; Stutzki & Güsten 1990; Lada, Bally, & Stark 1991; see also review by Salo 1985) are in the range 1.0–2.0. Even though the uncertainty in our derived power-law index is quite large because of the small number of cores in our sample, it seems reasonable to analyze the observational selection effects which can influence the analysis of the NH_3 core mass spectrum.

1. *Lower limit to mass sensitivity.* This lower limit can significantly flatten the slope of a mass spectrum. For our NH_3 observations, the lower limit is determined by our brightness temperature sensitivity, spatial and velocity resolution, and the limitations imposed by our core selection criterion (§ 4.1). A beam-sized 3 σ core which spans two channels in our observations and is optically thin with an NH_3 excitation temperature of 10 K and an NH_3 abundance of 10^{-8} would have a total NH_3 column density of 1.7×10^{15} cm^{-2} and a mass of 10 $M_\odot$. Since there is no significant flattening of the power law near this limit in Figure 13*b*, this selection effect does not appear to explain the relatively flat power law we derive.

2. *Multicomponent cores.* As noted in § 4, several of the NH_3 cores we have identified may actually be composed of several components. For example, DR 21 (OH) N may possess five or more individual components. Since each component of an NH_3 core must have a smaller mass than the core itself, it is quite possible that our core selection process has preferentially chosen the more massive cores. This kind of biasing will tend to flatten the mass spectrum power law. Therefore, our derived power-law exponent of 0.7 is a lower limit to the true power-law exponent. Low spatial resolution observations of other star-forming regions are also subject to this bias. Therefore, since all other derivations of the mass spectrum power law are based upon low spatial resolution studies, they must also be considered as lower limits to the true power-law exponent.

Beyond these two observational selection effects, one must also consider the breakdown in our basic assumptions used to derive the core masses: constant abundance and LTE. Potentially the most damaging of these would be the existence of abundance variations in DR 21 (OH). Several well-studied regions (L183; Swade 1989; Orion-KL: Mangum et al. 1990; see also review by Goldsmith 1992) are known to possess molecular abundance variations of up to several orders of magnitude. Therefore, it is reasonable to suspect such abundance variations in DR 21 (OH). Further high-resolution studies of DR 21 (OH) will quantify this suspicion.

6.2. *Comparison with Other Star-forming Regions*

Incongruities between our measurements of the NH_3 core physical properties in DR 21 (OH) and similar measurements in other star-forming regions do not allow a detailed comparison to be made. One property that we can compare, by using high spatial resolution ($\theta \lesssim 0.1$ pc) NH_3 observations of Taurus, OMC-1/OMC-2, and DR 21 (OH) is the core virial mass. We find that OMC-1/OMC-2 (M = 5 to greater than 100 $M_\odot$; Batrla et al. 1983) and DR 21 (OH) (M = 9–540 $M_\odot$; this work) contain primarily high-mass ($M > 50\ M_\odot$) molecular cores, while Taurus (M = 0.3–33 $M_\odot$; Benson & Myers 1989) is composed of low-mass ($M < 50\ M_\odot$) cores. Note that the upper bound to the virial mass in Taurus is likely not to be underestimated, given the completeness of the sample from which it was derived. This core virial mass comparison, coupled with the fact that OMC-1/OMC-2 and DR 21 (OH) appear to be producing primarily high-mass stars (see Paper I) while Taurus produces primarily low-mass stars, suggests that core mass can be used to distinguish between these two types of star formation.

7. CONCLUSIONS

Observations of the thermal NH_3(1, 1) and (2, 2) and H_2O maser emission toward the DR 21 (OH) molecular cloud have defined the detailed spatial and kinematic structure in this active star-forming region. The gas condensations which compose a 2′ section of the DR 21 (OH) molecular ridge surrounding the OH maser source range in size from 4″ to 19″, have gas masses in the range 14–1000 $M_\odot$, and range in kinetic temperature from 20 to higher than 80 K. Two of these condensations, designated MM 1 and MM 2, are associated with H_2O "shell-type" maser emission. MM 1, which is also the most intense NH_3 emission source in the region shows kinematic motions which may be due to rotation, infall, or outflow.

The high resolution and signal-to-noise ratio of our NH_3(1, 1) and (2, 2) measurements have allowed us to suggest two concepts describing the structure of the dense gas in DR 21 (OH). Both concepts involve the dynamical interaction between young forming stars and their environment, similar to the interaction observed in the AFGL 2591, M17, and Monoceros R2 star-forming regions.

In Paper I we found that the MM 1/MM 2 and DR 21 (OH) S components of the region possess size and luminosity characteristics intermediate between the Ophiuchus molecular core and the Kleinmann–Low Nebula of the Orion molecular cloud. Comparison between the core virial masses in Taurus, OMC-1/OMC-2, and DR 21 (OH) points to a connection between core virial mass and the type of star formation occurring in these regions. We find that core virial mass may represent the fundamental property which detemines whether a region is dominated by high- or by low-mass star formation.

J. G. M. would like to thank the National Radio Astronomy Observatory for support through a Junior Research Associateship. We also thank the referee, Neal Evans, for his helpful comments, which improved the text. This work was supported in part by Texas Advanced Research Program grant 003658-285 and National Science Foundation grant AST-9017710 to the University of Texas.

APPENDIX

In the following we discuss the methods used for calculating optical depth, column density, excitation temperature, and kinetic temperature from observations of the (1, 1) and (2, 2) transitions of NH_3. In the following discussion, adopting the notation of Ho et al. (1979), we will use J to denote the total angular momentum quantum number, K to denote the component of J along the

molecular axis of symmetry, m to denote the main hyperfine component in an inversion transition, and s to denote the other (satellite) hyperfine components of an inversion transition. For parallel discussions regarding these calculations, see Ho et al. (1979), Walmsley & Ungerechts (1983), and Stutzki & Winnewisser (1985).

A1. OPTICAL DEPTH

To calculate the optical depth $\tau(J, K, m)$ in the main hyperfine component of an NH_3 inversion transition, we assume that the beam filling factors and excitation temperatures for all hyperfine transitions are equal and in local thermodynamic equilibrium (LTE). This allows us to compare directly measurements of the hyperfine brightness temperatures:

$$\frac{T_B(J, K, m)}{T_B(J, K, s)} = \frac{1 - \exp\left[-\tau(J, K, m)\right]}{1 - \exp\left[-a\tau(J, K, m)\right]}, \tag{A1}$$

where

$$a \equiv \frac{\text{Intensity of satellite hyperfine transition}}{\text{Intensity of main hyperfine transition}}$$

(a is sometimes called the "transition intensity"). Using the relative intensity relations given in Townes & Schawlow (1955), we find that $a = 0.27778$ for the (1, 1) $F = 1 \rightarrow 2$ and $2 \rightarrow 1$ hyperfine components, 0.22222 for the (1, 1) $F = 1 \rightarrow 0$ and $0 \rightarrow 1$ hyperfines, 0.06520 for the (2, 2) $F = 2 \rightarrow 3$ and $3 \rightarrow 2$ hyperfines, and 0.06281 for the (2, 2) $F = 2 \rightarrow 1$ and $1 \rightarrow 2$ hyperfines. Therefore, defining

$$R \equiv \frac{T_B(J, K, m)}{T_B(J, K, s)},$$

equation (A1) reduces to

$$R\{1 - \exp\left[-a\tau(J, K, m)\right]\} + \exp\left[-\tau(J, K, m)\right] - 1 = 0. \tag{A2}$$

Solutions to equation (A2) yield the main hyperfine component optical depth $\tau(J, K, m)$.

In general, the hyperfine components of inversion transitions other than (1, 1) are not strong enough to be detected. In this case, to calculate the optical depth in the main hyperfine component of the (J', K') transition, one uses a slightly modified version of equation (A1):

$$\frac{T_B(J, K, m)}{T_B(J', K', m)} = \frac{1 - \exp\left[-\tau(J, K, m)\right]}{1 - \exp\left[-\tau(J', K', m)\right]}, \tag{A3}$$

assuming equal excitation temperatures and beam filling factors in the (J, K) and (J', K') transitions. Solving equation (A3) for $\tau(J', K', m)$,

$$\tau(J', K', m) = -\ln\left[1 - \frac{T_B(J', K', m)}{T_B(J, K, m)}\{1 - \exp\left[-\tau(J, K, m)\right]\}\right]. \tag{A4}$$

A2. AMMONIA COLUMN DENSITY

To derive the molecular column density, note that the total optical depth in a molecular transition, τ, is related to the number of molecules in the upper energy state of that transition, $\mathcal{N}_u$, by

$$\int \tau\, dv = \frac{8\pi^3 |\mu_{ul}|^2 \mathcal{N}_u}{3h}\left[\exp\left(\frac{hv}{kT_{ex}}\right) - 1\right], \tag{A5}$$

where, for NH_3, u and l refer to the upper and lower parity levels of an inversion transition, $|\mu_{ul}|^2$ is the molecular dipole moment matrix element, and the other terms have their usual meanings. For an NH_3 transition (J, K), $\mu = 1.468$ debye (Townes & Schawlow 1955),

$$|\mu_{ul}|^2 = \frac{\mu^2 K^2}{J(J+1)} \qquad \text{[for metastable } (J = K) \text{ transitions]},$$

and

$$\mathcal{N}_u = \frac{\exp\left(-hv/kT_{ex}\right)}{1 + \exp\left(-hv/kT_{ex}\right)} N(J, K). \tag{A6}$$

Therefore, equation (A5) becomes

$$\begin{aligned} N(J, K) &= \frac{3hJ(J+1)}{8\pi^3\mu^2K^2}\left[\frac{1 + \exp\left(-hv/kT_{ex}\right)}{1 - \exp\left(-hv/kT_{ex}\right)}\right]\int \tau(J, K)dv \\ &= 3.96 \times 10^{12}\,\frac{J(J+1)}{K^2}\left[\frac{1 + \exp\left(-hv/kT_{ex}\right)}{1 - \exp\left(-hv/kT_{ex}\right)}\right]\tau(J, K)\Delta v \text{ cm}^{-2}, \end{aligned} \tag{A7}$$

where $N(J, K)$ is the column density in both levels of the (J, K) inversion transition, $\tau(J, K)$ is the peak total (sum over all hyperfine components) optical depth in the inversion transition, Δv is the velocity width of the transition in kilometers per second, and T_{ex} is the excitation temperature in kelvins. Note that in equation (A7) a correction factor of $\{2[(\ln 2)/\pi]^{1/2}\}^{-1}$ has been applied to account for an assumed Gaussian line profile. Since it is more convenient to measure the optical depth in the main hyperfine component and use it to calculate $N(J, K)$, we use the following relation between $\tau(J, K)$ and $\tau(J, K, m)$:

$$\tau(J, K) = \left[\sum^{F,F'} (\mathrm{RI})_{F,F'} \Big/ \sum^{F,F'} (\mathrm{RI})_m\right] \tau(J, K, m) , \tag{A8}$$

where RI is the relative intensity for a quadrupole hyperfine component. For the (1, 1) and (2, 2) transitions,

$$I_{JK} \equiv \left[\sum^{F,F'} (\mathrm{RI})_{F,F'} \Big/ \sum^{F,F'} (\mathrm{RI})_m\right] = \begin{cases} 2.000 & \text{for } (1, 1) , \\ 1.256 & \text{for } (2, 2) , \end{cases}$$

and equation (A7) becomes

$$N(J, K) = 3.96 \times 10^{12} \frac{J(J+1)}{K^2} \left[\frac{1 + \exp(-h\nu/kT_{ex})}{1 - \exp(-h\nu/kT_{ex})}\right] I_{JK} \tau(J, K, m) \Delta v \ \mathrm{cm}^{-2} . \tag{A9}$$

We can further reduce this expression by noting that $h\nu/k \simeq 1.2$ K for the astrophysically important inversion transitions. Therefore, using the approximation that $h\nu \ll kT_{ex}$, equation (A9) becomes

$$N(J, K) = 1.65 \times 10^{14} \frac{J(J+1)T_{ex}}{K^2 \nu} I_{JK} \tau(J, K, m) \Delta v \ \mathrm{cm}^{-2} , \tag{A10}$$

where ν is the transition frequency in GHz and Δv is the velocity width in kilometers per second. For the (1, 1) and (2, 2) transitions, equation (A10) becomes

$$N(1, 1) = 6.60 \times 10^{14} \frac{T_{ex}(2, 2; 1, 1)}{\nu(1, 1)} \tau(1, 1, m) \Delta v \ \mathrm{cm}^{-2} \tag{A11}$$

$$N(2, 2) = 3.11 \times 10^{14} \frac{T_{ex}(2, 2; 1, 1)}{\nu(2, 2)} \tau(2, 2, m) \Delta v \ \mathrm{cm}^{-2} , \tag{A12}$$

where, as in equation (A3), we assume $T_{ex}(1, 1) = T_{ex}(2, 2) = T_{ex}(2, 2; 1, 1)$ (see § A.3 below).

The total NH_3 column density, $N_{TOT}(NH_3)$, can be calculated using the following:

$$N_{TOT}(NH_3) = \frac{N(J, K) Q_{ROT}}{(2J+1) g_I g_K} \exp\left[\frac{E(J, K)}{T_{ex}(J', K'; J, K)}\right] , \tag{A13}$$

where g_I is the nuclear spin degeneracy, g_K is the K-degeneracy, $E(J, K)$ is the energy of the inversion state above the ground state in kelvins, and the rotational partition function Q_{ROT}, is given by

$$Q_{ROT} \equiv \sum_J \sum_K (2J+1) g_I g_K \exp\left[-\frac{E(J, K)}{T_{ex}(J', K'; J, K)}\right] . \tag{A14}$$

A plot of Q_{ROT} as a function of T_{ex} is given in Figure 14.

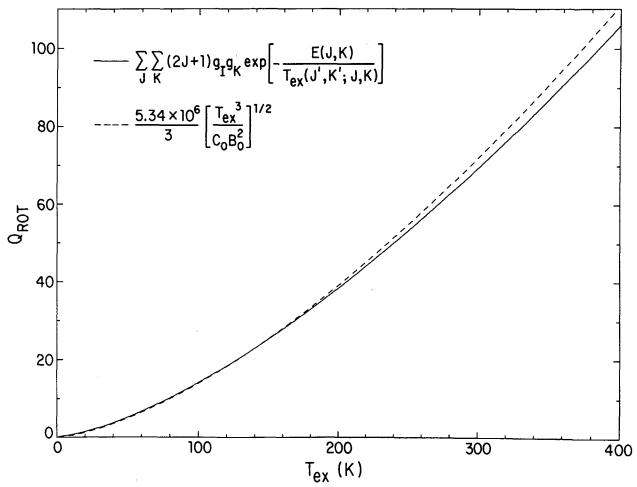

FIG. 14.—Rotational partition function for NH_3. The solid line is the partition function calculated using eq. (A14), which includes 248 energy levels up to 3496 K in excitation. The dashed line represents the partition function calculated using the standard high-temperature approximation (see Gordy & Cook 1970, p. 57).

A3. EXCITATION AND KINETIC TEMPERATURE

If the metastable states in NH_3 are coupled only through collisions, and the populations in the upper states in each K-ladder ($J \neq K$) can be neglected, the populations in the metastable states are related through the Boltzmann equation. In molecular clouds, though, $\Delta K = 1$ collisions across K-ladders will deplete metastable states in favor of their next lower J metastable states. Therefore, for example, collisional de-excitation of the (2, 2) transition will result in an increase in the population of the (2, 1) state, followed by quick radiative relaxation of the (2, 1) state into the (1, 1) state. This implies that an excitation temperature, $T_{ex}(J', K'; J, K)$, relating the populations in the (J', K') and (J, K) states, $n(J', K')$ and $n(J, K)$, may be derived. From the Boltzmann equation,

$$\frac{n(J', K')}{n(J, K)} = \frac{g(J', K')}{g(J, K)} \exp\left[- \frac{\Delta E(J', K'; J, K)}{T_{ex}(J', K'; J, K)} \right],$$

equations (A5) and (A6) [assuming $hv \ll kT_{ex}(J', K'; J, K)$] for the (J, K) and (J', K') transitions,

$$\frac{N(J', K')}{N(J, K)} = \frac{J'(J' + 1)K^2\tau(J', K')\Delta v(J', K')}{J(J + 1)(K')^2\tau(J, K)\Delta v(J, K)},$$

and the fact that in a homogeneous molecular cloud

$$\frac{n(J', K')}{n(J, K)} = \frac{N(J', K')}{N(J, K)},$$

we find that

$$\frac{g(J', K')}{g(J, K)} \exp\left[- \frac{\Delta E(J', K'; J, K)}{T_{ex}(J', K'; J, K)} \right] = \frac{J'(J' + 1)K^2\tau(J', K')\Delta v(J', K')}{J(J + 1)(K')^2\tau(J, K)\Delta v(J, K)}. \quad \text{(A15)}$$

Using equation (A8) to relate the total optical depth $\tau(J, K)$ to the optical depth in the main hyperfine component $\tau(J, K, m)$, noting that for NH_3 $g(J, K) = 2J + 1$, and solving equation (A15) for $T_{ex}(J', K'; J, K)$ we find that

$$T_{ex}(J', K'; J, K) = - \Delta E(J', K'; J, K) \left\{ \ln\left[\frac{(2J + 1)J'(J' + 1)K^2 I_{J'K'}\tau(J', K', m)\Delta v(J', K')}{(2J' + 1)J(J + 1)(K')^2 I_{JK}\tau(J, K, m)\Delta v(J, K)} \right] \right\}^{-1}. \quad \text{(A16)}$$

Using equation (A4), equation (A16) becomes

$$T_{ex}(J', K'; J, K) = -\Delta E(J', K'; J, K) \times \left[\ln\left(\frac{(2J + 1)J'(J' + 1)K^2 I_{J'K'}\Delta v(J', K')}{(2J' + 1)J(J + 1)(K')^2 I_{JK}\tau(J, K, m)\Delta v(J, K)} \ln\left[1 - \frac{T_B(J', K', m)}{T_B(J, K, m)} \{1 - \exp[-\tau(J, K, m)]\} \right] \right) \right]^{-1}. \quad \text{(A17)}$$

For $(J', K') = (2, 2)$ and $(J, K) = (1, 1)$ equation (A17) becomes

$$T_{ex}(2, 2; 1, 1) = -41.5 \left[\ln\left(- \frac{0.283\Delta v(2, 2)}{\tau(1, 1, m)\Delta v(1, 1)} \ln\left[1 - \frac{T_B(2, 2, m)}{T_B(1, 1, m)} \{1 - \exp[-\tau(1, 1, m)]\} \right] \right) \right]^{-1}. \quad \text{(A18)}$$

To derive the gas kinetic temperature from $T_{ex}(2, 2; 1, 1)$, one uses statistical equilibrium (noting that only collisional processes are allowed between the different K-ladders), detailed balance, and the Boltzmann equation to calculate T_K from $T_{ex}(J', K'; J, K)$. Assuming that the populations in the (1, 1) and (2, 2) transitions are much greater than that in the higher lying levels of para-NH_3 and that the population of the nonmetastable (2, 1) level is negligible in comparison with that in the (1, 1) level, we can use this "three-level model" of NH_3 to analytically derive an expression relating $T_{ex}(2, 2; 1, 1)$ and T_K:

$$1 + \frac{C(2, 2; 2, 1)}{C(2, 2; 1, 1)} = \left\{ \frac{g(1, 1)}{g(2, 2)} \exp\left[\frac{\Delta E(2, 2; 1, 1)}{T_{ex}(2, 2; 1, 1)} \right] \right\} \left\{ \frac{g(2, 2)}{g(1, 1)} \exp\left[- \frac{\Delta E(2, 2; 1, 1)}{T_K} \right] \right\}, \quad \text{(A19)}$$

where $C(J', K'; J, K)$ is the collisional excitation rate at temperature T_K between levels (J', K') and (J, K). Equation (A19) can be rewritten as

$$T_{ex}(2, 2; 1, 1) \left\{ 1 + \left(\frac{T_K}{41.5} \right) \ln\left[1 + \frac{C(2, 2; 2, 1)}{C(2, 2; 1, 1)} \right] \right\} - T_K = 0. \quad \text{(A20)}$$

Solutions of this equation give T_K for a measured $T_{ex}(2, 2; 1, 1)$.

REFERENCES

Bally, J., & Lada, C. J. 1983, ApJ, 265, 824
Batrla, W., Wilson, T. L., Bastien, P., & Ruf, K. 1983, A&A, 128, 279
Benson, P. J., & Myers, P. C. 1989, ApJS, 71, 89
Blitz, L. 1987, in Physical Processes in Interstellar Clouds, ed. G. G. Morfill & M. Scholer (Dordrecht: Reidel), 35
Campbell, M. F., Hoffmann, W. F., Thronson, H. A., Jr., Niles, D., Nawfel, R., & Hawrylycz, M. 1982, ApJ, 261, 550
Casoli, F., Combes, F., & Gérin, M. 1984, A&A, 133, 99
Danby, G., Flower, D. R., Valiron, P., Schilke, P., & Walmsley, C. M. 1988, MNRAS, 235, 229

Downes, D., & Rinehart, R. 1966, ApJ, 144, 937
Fischer, J., Sanders, D. B., Simon, M., & Solomon, P. M. 1985, ApJ, 293, 508
Garden, R., Geballe, T. R., Gatley, I., & Nadeau, D. 1986, MNRAS, 220, 203
Gear, W. K., Chandler, C. J., Moore, T. J. T., Cunningham, C. T., & Duncan, W. D. 1988, MNRAS, 231, 47P
Genzel, R. 1989, private communication
Genzel R., & Downes, D. 1977, A&A, 61, 117
Goldsmith, P. F. 1992, in IAU Symp. 147, Fragmentation and Small-Scale Structure in Molecular Clouds (New York: Springer), in press
Gordy, W., & Cook, R. L. 1970, Microwave Molecular Spectra (New York: Wiley)
Harris, S. 1973, MNRAS, 162, 5P
Harvey, P. M., Joy, M., Lester, D. F., & Wilking, B. A. 1986, ApJ, 300, 737
Ho, P. T. P., Barrett, A. H., Myers, P. C., Matsakis, D. N., Cheung, A. C., Chui, M. F., Townes, C. H., & Yngvesson, K. S. 1979, ApJ, 234, 912
Johnston, K. J., Henkel, C., & Wilson, T. L. 1984, ApJ, 285, L85
Kukolich, S. G. 1967, Phys. Rev., 156, 83
Lada, C. J. 1985, ARA&A, 23, 267
Lada, E. A., Bally, J., & Stark, A. A. 1991, ApJ, 368, 432
Lane, A. P., Haas, M. R., Hollenbach, D. J., & Erickson, E. F. 1990, ApJ, 361, 132
Loren, R. B. 1989, ApJ, 338, 902
Mangum, J. G., Wootten, A., Loren, R. B., & Wadiak, E. J. 1990, ApJ, 348, 542
Mangum, J. G., Wootten, A., & Mundy, L. G. 1991, ApJ, 378, 576 (Paper I)
Massi, M., Churchwell, E., & Felli, M. 1988, A&A, 194, 116
Matsakis, D. N., Brandshaft, D., Chui, M. F., Cheung, A. C., Yngvesson, K. S., Cardiasmenos, A. G., Shanley, J. F., & Ho, P. T. P. 1977, ApJ, 214, L67
Mauersberger, R., Henkel, C., Wilson, T. L., & Walmsley, C. M. 1986, A&A, 162, 199
Mauersberger, R., Wilson, T. L., Batria, W., Walmsley, C. M., & Henkel, C. 1985, A&A, 146, 168
Norris, R. P., Booth, R. S., Diamond, P. J., & Porter, N. D. 1982, MNRAS, 201, 191
Padin, S., et al. 1989, ApJ, 337, L45
Panagia, N. 1973, AJ, 78, 929
Phillips, T. G., Huggins, P. J., Wannier, P. G., & Scoville, N. Z. 1979, ApJ, 231, 720
Plambeck, R. L., & Menten, K. A. 1990, ApJ, 364, 555
Reid, M. J., Muhleman, D. O., Moran, J. M., Johnston, K. J., & Schwartz, P. R. 1977, ApJ, 214, 60
Reid, M. J., Schneps, M. H., Moran, J. M., Gwinn, C. R., Genzel, R., Downes, D., & Rönnäng, B. 1988, ApJ, 330, 809
Richardson, K. J., Sandell, G., & Krisciunas, K. 1989, A&A, 224, 199
Roelfsema, P. R., Goss, W. M., & Geballe, T. R. 1989, A&A, 222, 247
Sandell, G. 1990, private communication
Sanders, D. B., Scoville, N. Z., & Solomon, P. M. 1985, ApJ, 289, 373
Scalo, J. M. 1985, in Protostars and Planets II, ed. D. C. Black & M. Shapley Mathews (Tucson: Univ. Arizona Press), p. 201
Stutzki, J., & Güsten, R. 1990, ApJ, 356, 513
Stutzki, J., & Winnewisser, G. 1985, A&A, 144, 13
Swade, D. A. 1989, ApJS, 71, 219
Thum, C., & Lemke, D. 1975, A&A, 41, 467
Torrelles, J. M., Ho, P. T. P., Rodríguez, L. F., & Cantó, J. 1989, ApJ, 343, 222
———. 1990, ApJ, 349, 529
Townes, C. H., & Schawlow, A. L. 1955, Microwave Spectroscopy (New York: Dover)
Walmsley, C. M., & Ungerechts, H. 1983, A&A, 122, 164
Wilson, T. L., & Mauersberger, R. 1990, A&A, 239, 305
Woody, D. P., Scott, S. L., Scoville, N. Z., Mundy, L. G., Sargent, A. I., Padin, S., Tinney, C. G., & Wilson, C. D. 1989, ApJ, 337, L41